Article:
Yu, X., Wang, C., Bertolini, G. et al. (2 more authors) (2025) Late Cretaceous glaciations in a hyper-arid plateau desert of the South China Coastal Mountains. Geological Society of America Bulletin, 137 (5-6). pp. 1891-1908. ISSN: 0016-7606

https://doi.org/10.1130/b37683.1

Late Cretaceous glaciations in a hyper-arid plateau desert of the South China Coastal Mountains

Xiaocan Yu[1,*], Chunlian Wang[2,*], Gabriel Bertolini[3], Nigel P. Mountney[4], Chao You[2,5]

[1]*Institute of Geology, Chinese Academy of Geological Sciences, Beijing 100037, China*

[2]*MNR Key Laboratory of Metallogeny and Mineral Assessment, Institute of Mineral Resources, Chinese Academy of Geological Sciences, Beijing 100037, China*

[3]*Instituto de Geociências, Universidade Federal do Rio Grande do Sul, Porto Alegre 90040-060, Brazil*

[4]*Fluvial, Eolian & Shallow-Marine Research Group, School of Earth and Environment, University of Leeds, LS2 9JT, Leeds, UK*

[5]*School of Earth and Space Sciences, Peking University, Beijing 100871, China*

*Corresponding author: xiaocany1988@163.com; wangchunlian312@163.com

ABSTRACT

Increasing evidence indicates the existence of a cryosphere during the Cretaceous supergreenhouse. However, current understanding of a potential link between lithosphere dynamics and cryospheric processes in the Cretaceous plateau desert successions of China remains limited. We report the occurrence of ice-rafted dropstones and diamictites from the Upper Cretaceous Chishan Formation of the Subei Basin at the East Asian continental margin. Results from the analysis of provenance indicate that fluvial deposits of the Lower Chishan Formation were mainly derived from the Sulu Orogen to the north and the Zhangbaling Uplift to the west, whereas aeolian deposits

of the Upper Chishan Formation were largely recycled from the two highlands, with an additional notable contribution from the post-Cretaceous basement of the Yangtze Block. Combined with previous evidence, provenance analysis indicates that Late Cretaceous collision between the Okhotomorsk Block and the East Asian continent led to the growth of the South China coastal mountains via crustal thickening, which generated an arid, high-altitude basin region that experienced desertification and paleohydrological variability, and that was supplied with additional clastic sediment sources from the basement. Our results provide evidence of Late Cretaceous cryospheric processes in a continental mid-latitude plateau desert linked to the north-westward subduction and collision of the paleo-Pacific realm. Global cooling from the late Turonian to Maastrichtian drove the establishment of glaciers in high-altitude mountains leading to the development of ice-related deposits in the plateau deserts, as recorded in the Subei desert basin of the South China Coastal Mountains. The record of ice-rafted debris and the provenance signature reveal an active Cretaceous plateau cryosphere linked to lithosphere dynamics.

INTRODUCTION

The distribution of climate zones in East Asia during the Cretaceous is closely associated with atmospheric circulation patterns and lithospheric tectonic forcing (Jiang et al., 2008; Hagegawa et al., 2012; Wu et al., 2022). Cryospheric conditions have bene shown to have operated at different time intervals during the Cretaceous supergreenhouse in East Asia. During the Early Cretaceous, ice sheets, glacial debris flows, ice-rafted deposits and sand wedges developed in the plateau region at

paleolatitudes of ~40°−45°N (Wang et al., 1996; Cheng et al., 2002; Yang et al., 2013; Wang et al., 2023). During the mid-Cretaceous, ice-rafted dropstones and diamictites occurred in the plateau desert basins at a paleolatitude of ~20°N (Wu and Rodríguez-López, 2021). During the Late Cretaceous, striated cobbles indicate temporary glacial events in an intermontane desert basin at a paleolatitudes of ~30°N (Jiao et al., 2020; Cao et al., 2023a). Thus, a growing body of sedimentological evidence suggests a Cretaceous plateau cryosphere in East Asia.

Fluvial–aeolian sedimentary successions record evidence of shifts between relatively wetter and drier climate regimes (Rodríguez-López et al., 2014; Lacotte and Mountney, 2022). In continental basins, arid conditions may facilitate the dominance of aeolian sedimentary processes, whereas fluvial systems are more active in response to wetter conditions. Numerous studies of ancient continental sedimentary successions have demonstrated a link between enhanced aeolian accumulation and a decrease in mean global temperature (e.g., Cosgrove et al., 2022; Rodríguez-López et al., 2022; Wu et al., 2022; Scherer et al., 2023). Wu and Rodríguez-López (2021) presented evidence of ice-related structures within aeolian interdune strata of mid-Cretaceous desert sedimentary successions in the Chuxiong and Simao basins of southwest China. However, it remains to be determined whether cryospheric processes were widespread during episodes of arid climate conditions in continental sedimentary basins during the Cretaceous period.

Deposits of ice-rafted debris are reported in several mid-Cretaceous desert depositional successions in south-western China and these are indicative of the

operation of cryospheric processes in a low-latitude in the Northern Hemisphere at this time (Wu and Rodríguez-López et al., 2021). In addition to recognition of a global cooling in the Late Cretaceous (Pucéat et al., 2003; Friedrich et al., 2012; Linnert et al., 2014), other local-to-regional factors, notably a substantial increase in paleo-altitude induced by orogenic processes (lithospheric forcing), could additionally act to enable glacial depositional processes in terrestrial sedimentary successions.

the aim of this work is to demonstrate evidence for continental cryospheric processes induced by paleoclimate and lithosphere dynamics at the East Asian continental margin. Specific objectives are as follows: (i) to describe the presence of dropstones and diamictites, along with the associated lithofacies, from the Upper Cretaceous Chishan Formation of the Subei desert basin of the South China margin; (ii) to characterize the cryospheric processes that operated during the Late Cretaceous in the mid-latitudes of the Northern Hemisphere; and (iii) to evaluate the influence of lithospheric dynamics on possible global Late Cretaceous glaciations by analysis of paleocurrent, petrography and detrital zircon U-Pb Geochronology data of Cretaceous rocks in the Subei Basin.

GEOLOGICAL BACKGROUND

The Subei basin is a Cretaceous to Cenozoic rift basin that developed along the East Asian continental margin (Chen et al., 2010). It is bounded by the Tan-Lu Fault to the west, the Jiangnan Orogen to the south, and the Sulu Orogen to the north (Fig. 1A). The Upper Cretaceous sedimentary successions of the basin fill include the Pukou, Chishan and Taizhou formations, from bottom to top. From analysis of ostracod,

charophyta and sporopollen assemblages, these formations are determined to be Cenomanian to Coniacian, Santonian to Campanian, and Maastrichtian in age, respectively (BGMRJ, 1997; Yue et al., 1997; Yue and Ding, 1999) (Table S1 in the Supplemental Material). The Chishan Formation is characterized by mixed fluvial–aeolian deposits and can be divided into the Lower and Upper members (Yue et al., 1997). The Lower section comprises purple-red sandstones, siltstones and mudstones (Fig. 1C). The Upper section comprises brick-red fine- to coarse sandstones with subordinate very fine sandstones, siltstones and mudstones, which represent alternating deposits of aeolian dunes and wet interdunes (Yue et al., 1997; Cao et al., 2023b) (Fig. 1C). Proposed ice-related deposits are located in the interdune deposits of the Upper unit, and are observed in the Dingyuan area in the western Subei basin (118°0′46″E, 32°36′41″N) (Fig. 1B and Fig. S1 in the Supplemental Material).

METHODS

Eight stratigraphic sections from the Chuzhou, Ma'anshan, Chishan, and Dingyuan regions in eastern China were examined (Fig. 2). Lithofacies analysis was undertaken to classify sedimentary characteristics of the Chishan Formation in the Subei basin. The recognition and identification of ice-related deposits in interdune facies builds upon findings from earlier studies by Rodríguez-López et al. (2008) and Wu and Rodríguez-López (2021). Paleocurrent data were obtained from measurements of the azimuth of foresets of small-scale (0.2−0.8 m thick) cross-bedded sets of aqueous origin (n=22), and of large-scale (1.5−10 m thick) cross-bedded dune foresets of aeolian origin (n=71). These data were corrected to remove post-Cretaceous crustal rotation via

analysis of paleomagnetic data (Sun et al., 2006), before being plotted on rose diagrams. Ten aeolian sandstone samples in the Upper member of the Chishan Formation and six aqueous sandstone samples in the Lower member were collected and analyzed using a Leica optical microscope to determine paragenetic associations, and to determine lithological composition using grain count methods. Based on the Gazzi-Dickinson point counting method (Dickinson and Suczek, 1979; Ingersoll et al., 1984), at least 300 framework grains were counted per thin section. Three aeolian sandstone samples in the Upper member of the Chishan Formation and three aqueous sandstone samples in the Lower member were chosen for the analysis of detrital zircon U-Pb geochronology. Kernel density estimate (KDE) diagrams with a bandwidth of 30 Myr were constructed to visualize the zircon U-Pb age frequency distribution using IsoplotR (Vermeesch, 2012, 2018; Vermeesch et al., 2016); the peak heights of younger groups of an age distribution are magnified by the probability density model. Plots of cumulative probability densities (CPD) were also applied as an addition to the KDE model. The complexity of the parent sources of clastic sediments in a continental basin makes it challenging to identify provenance information. Thus, multidimensional scaling (MDS) was applied to transform dissimilarity quantification into a single point on a scatter plot for comparing multiple sources using the DZmds software program (Vermeesch, 2013; Saylor and Sundell, 2016). X-ray diffraction analysis was performed on twelve mudstone samples in the Upper member of the Chishan Formation to identify and quantify the clay minerals. The detailed analytical procedures and data results are listed in the Supplemental Material.

FACIES ASSOCIATIONS

Nine lithofacies have been identified based on analysis of the sedimentology of the Chishan Formation. These lithofacies record evidence of aqueous and aeolian processes. They form eight facies associations that make up architectural elements. Key characteristics of each architectural element are summarized in Table 1.

Aeolian dune

This facies association is composed of well-sorted coarse- to very fine-grained sandstones (Ste) arranged into tabular or trough cross-stratified sets, 0.15 to 10 m thick. These light pink sandstones show sharp planar or subhorizontal upper and lower surfaces. Internal stratification in the cross-bedded sets records grainflow, wind-ripple and grainfall processes (Fig. 3). Translatent wind-ripple laminae occur in the basalmost ** m of the cross-stratified sets. They are characterized by millimeter-scale inversely graded laminae. Grainflow strata are the primary component of the foresets of the cross-stratified sets. Laminae are inversely graded or massive and may occur intercalated with wind-ripple laminae (Figs. 3A−3C). Grainfall strata are represented by millimeter-scale laminae of fine sandstone that commonly occur between individual grainflow deposits (Fig. 3D). The azimuths of the foresets are mainly between 035° and 100°, but subordinately range from 195° to 235°.

The large-scale cross-bedding consisting of grainflow, wind-ripple and grainfall strata suggests the deposition upon aeolian dunes (Hunter, 1977). The dominant occurrence of grainflow strata indicates the presence of well-developed slipfaces in the wind direction (Kocurek, 1991). The grain flow strata packages resulted from the

predominant westerly and subordinate northeasterly winds. The relative divergence between foreset azimuths and low-angle-inclined bounding surfaces indicates migrating crescentic dunes with sinuous crestlines (Rubin, 1987; Kocurek, 1991).

Interdune facies association

This facies association consists of purple mudstones (Fl), very fine sandstones (Sm), structureless muddy sandstones (Ss), and well-sorted laminated sandstones (She). Elements of this association form a decimeter-thick body with a lenticular geometry that pinches out between the cross-bedded aeolian dune elements laterally (Figs. 4 and 5A). The architectural arrangement commonly records an intertonguing relationship with the toesets of the overlying aeolian dune cross-strata.

Rounded to subrounded mud intraclasts (Figs. 5B−5E) occur in this facies association. They have widths of 0.8−22.8 cm and lengths of 1.0−31.7 cm. The clay minerals in these mud intraclasts are characterized by 83−90% illite/smectite mixed layers and 9−17% illite (Table S2). Examples of lonestones and diamictons within this facies association are observed. Lonestones are formed by isolated mud pebbles or cobbles “floating” entirely encased within an aeolian sandstone matrix (Figs. 5F−5H). Lonestones have lengths of 1.5−15 cm and widths of 1−7 cm. Lonestones are common within host sediments: these hosting laminated sandstones show rupture, penetration and bending structures in strata directly beneath the lonestones, and onlapping and bending structures directly atop (Figs. 5F−5I). The clay minerals in these lonestones consist of illite/smectite mixed layers (83−88%) and subordinate illite (9−16%) (Table S2). The diamictons are formed by rounded to subrounded mud pebbles and cobbles

177 that possess a lenticular or thin-bedded geometry (Figs. 5J−5M), cm- to m-scale thick.
178 These diamictons disrupt and deform the laminated sandstones on which they lie; they
179 are draped by the overlying wind-ripple lamination (Figs. 5J−5M). The shape of the
180 mud pebbles and cobbles in the diamicton is similar to the shape of the mud intraclasts
181 associated with wet interdune deposits (Figs. 4A and 5B−5E). These lonestones and
182 diamictons display distinguishing features indicative of vertical or oblique fall into the
183 host sediment (Figs. 5F−5M). The clay minerals in these diamictons comprise
184 illite/smectite mixed layers (84−89%) and subordinate illite (10−13%) (Table S2).

185 The presence of the decimeter-thick lens-shaped geometry interbedded with
186 aeolian dune cross-strata suggests deposition of aeolian interdunes (Kocurek, 1981;
187 Mountney and Thompson, 2002). The well-sorted laminated sandstones are wind-ripple
188 strata implying a dry interdune where the water table was below the depositional surface
189 (Kocurek, 1981). The structureless muddy sandstones define deposition in a damp
190 interdune where the groundwater level reached the depositional surface that captured
191 windblown dust and sand grains (Kocurek, 1981). The lenticular geometry consisting
192 of mudstones or interbedded sandstones and mudstones indicates a wet interdune
193 element that developed in areas where the interdune depressions suffered fluvial floods
194 (Kocurek, 1981; Mountney and Thompson, 2002).

195 The preserved aeolian architectures demonstrate the intertonguing of the toesets
196 of dunes and adjacent near-horizontal strata of coevally active interdunes, similar in
197 form to those reported in the mid-Cretaceous desert in southwestern China and Iberia
198 (Rodríguez-López et al., 2012; Wu and Rodríguez-López, 2021). The relationship

demonstrates that mud intraclasts were derived locally from wet interdune deposits (cf. Rodríguez-López et al., 2008). The mud intraclasts typically have a rounded to subrounded shape. However, the manner of draping of overlying sandstone deposits over the mudstone clasts indicates that the clast-shaping process was not caused by water transport but by a process of essentially in-situ deformation due to the compaction of overlying aeolian dune toeset sandstones that caused the mud layer to be pinched. Differential compaction between aeolian dune sandstones and wet interdune deposits generated the mud pebbles and cobbles, which occur at the same stratigraphic level as adjacent undeformed parent interdune deposits. The formation mechanism is similar to that proposed by Wu and Rodríguez-López (2021) for deposits in oases of the Badain Jaran Desert, China: sediment loading under freezing conditions led to the compaction-induced formation of mud intraclasts in the interdune facies (Fig. 6A). Ice floe at the margins of the oases resulted in reworking, loosening, transport and re-deposition of these mud intraclasts (Fig. 6B).

The geometries of these lonestones are similar to dropstones reported from the mid-Cretaceous desert basins in southwestern China (Wu and Rodríguez-López, 2021), where falling mud intraclasts cause disruption and warping of the hosting laminated sandstones (Fig. 6C). The occurrence of the intraclasts in aeolian successions is commonly associated with water incursion into low-lying, low-relief parts of coastal or inland erg margin systems (Rodríguez-López et al., 2012). In this research, these mud intraclasts are all associated with wet interdune deposits. The similarity in clast shape and composition, and the presence of compaction-induced mudstone features in the wet

interdune facies indicate that these lonestones and diamictons are derived from the mud intraclasts in the wet interdune deposits. Moreover, the geometrical relationships of the lonestones and diamictons and their relationship to their host sediments in the Subei aeolian deposits are similar to ice-rafted dropstones occurring in other ancient strata (e.g., Rodríguez-López et al., 2016; Le Heron et al., 2017; Wu and Rodríguez-López, 2021; Xia et al., 2023).

Aeolian sandsheet

This facies association consists of well-sorted horizontal to sub-horizontal laminated fine sandstones (She). These light pink tabular sandstones are 1.5 m to 9 m thick and several to tens of meters wide (Figs. 7A and 7B). Internal stratification is characterized by subcritically climbing translatent strata 1–8 mm thick with inverse grading (Fig. 7C). This facies association occurs alone or interlayered with wet interdunes or aeolian dunes. The dip directions of the low-angle cross-bedding range from 6° to 12° and 332° to 340°.

The tabular packages of horizontal to low-angle laminae suggest aeolian deposition (Hunter, 1977; Kocurek, 1981). The subcritically climbing translatent strata represent the migrating wind ripples (Hunter, 1977). They commonly occur in dry interdune, dune plinth and aeolian sheet deposits (Kocurek, 1981; Clemmensen, 1989; Mountney and Thompson, 2002). Given the large thickness and lateral extent and the isolated occurrence of this architectural element, this facies association is interpreted as aeolian sheet facies.

Fluvial channel deposits

This facies association is composed of trough cross-bedded sandstones (St), low-angle cross-bedded sandstones (Sl) and thinly bedded or lenticular purple mudstones (Fl) (Figs. 8A and 8B). These sand bodies extend for several meters to tens of meters laterally and are bounded by low-relief basal erosional surfaces. The sandstones and mudstones form fining-upward units. The dip directions of the low-angle and trough cross-bedding are between 085° and 115°.

The dominance of the fining-upward units with erosive bases suggests fluvial channel deposits (Miall, 1977). The trough cross-bedded sandstones are the products of downstream migration of sand bars in channels (Miall, 1977; Todd, 1989). The good development of sandstones with trough and low-angle cross-bedding, along with the extensive tabular sand bodies bounded by erosional bases, indicates that this facies was formed in ephemeral fluvial channel settings (Allen et al., 2014).

Overbank flood deposits

This facies association comprises massive tabular sandstones (Sm) and laminated mudstones (Fl) without erosive bases (Figs. 8C and 8D). The tabular heterolithic units are decimeter thick and several meters to tens of meters wide. Pale grey-green mottling, silty aggregates and slickensides are observed in the meter-scale thick massive mudstone layers.

The presence of interbedded massive tabular sandstones and laminated mudstones with no erosive bases indicates unconfined flow deposition that characterizes overbank flood deposits (Smith et al., 1989; Miall, 1996). The fining-upward units record successive waning flood events (Smith et al., 1989). The occurrence of red coloration,

mottling, silty aggregates and slickensides in the thick mudstone layers suggests oxidizing conditions and pedogenic alteration, and that floodplain environments could have formed during high-magnitude floods (Retallack, 1994; Basilici et al., 2022).

Lake deposits

This facies association consists of siltstones and mudstones (Fl), with massive muddy sandstones (Sm) and minor horizontal to low-angle cross-bedded laminated sandy conglomerates (Gh) and lenticular low-angle cross-bedded sandstones (Sl). Two types of lithological assemblages are formed. The first is interbedded massive mudstones and laminated siltstones several meters thick and tens of meters wide (Fig. 9A). The second is vertical packages of siltstones and mudstones with laminated sandy conglomerates, massive muddy sandstones and low-angle cross-bedded sandstones (Figs. 9B−9D). Fossilized root traces are observed at the base of massive sandstones (Fig. 9C). Burrows are developed in the fine sediments (Fig. 9D). Mudcracks are also observed atop the muddy sandstones (Fig. 9E). These fine sediments contain abundant ostracodes and charophytes (Yue et al., 1997). The dip directions of the low-angle cross-bedding vary from 138° to 175°.

The dominance of massive mudstones and thin-bedded siltstones is indicative of a shallow lake setting (Benvenuti, 2003; Scherer et al., 2007). The presence of fossilized root traces, burrows, ostracodes, and charophytes suggests a lacustrine environment (Van Itterbeeck et al., 2007). The laminated sandy conglomerates, massive muddy sandstones and low-angle cross-bedded sandstones are formed in the lake marginal environment due to the deceleration of streams as they flow into a lake (Frisch et al.,

2019). The presence of mudcracks indicates periodic exposure of the lake marginal areas.

PROVENANCE SIGNATURES

Paleocurrent analysis

Paleocurrent measurements were conducted to reveal regional and temporal paleocurrent orientations (Fig. 2). Paleocurrent data obtained from aqueous cross-beds of the Lower Chishan Formation indicate a southeastward paleo-water flow, implying the sources to the north and the west. Paleocurrent orientations obtained from large-scale cross-bedded dune foresets of aeolian origin indicate dominant westerlies followed by northeasterlies and minor southeast winds, which are consistent with Late Cretaceous paleowind pattern that existed in the middle and low latitudes of the Northern Hemisphere (Jiang et al., 2008; Hagegawa et al., 2012; Yu et al., 2021).

Petrographic indicators

All examined sandstone samples from the Subei basin have a quartz−lithic composition with minor feldspar grains (Fig. 10A; Table S3). The detrital grains are subangular to well-rounded. Quartz grains are the most prevalent component and account for a mean of 76% from the framework. Distinct monocrystalline quartz grains with uniform extinction occur in all samples. Feldspar grains of the total rock composition are less than 5%. Plagioclase content is greater than that of K-feldspar and constitutes 70−90% of the total feldspars. Lithic fragments of the framework represent 21%, on average. These lithic fragments are dominated by metamorphic quartzite (56−90% of the total lithic fragments), with subordinate volcanic and sedimentary lithic

grains.

Sandstone samples in the Lower member of the Chishan Formation contain relatively high amounts of sedimentary lithic fragments consisting of mudstone, siltstone, chert and carbonate (Figs. 10G−10I; Table S3), whereas those in the Upper member comprise distinctive volcanic clasts characterized by felsic textures (Figs. 10D−10F; Table S3).

Most of the monocrystalline quartz grains are clear and free of inclusions; they occasionally have embayment textures (Figs. 10D−10I). The presence of these textures suggests a volcanic origin (Yan et al., 2010). The occurrence of the monocrystalline quartz grains with inclusions and uniform extinction, and of the potassium feldspar grains indicates a felsic igneous source (Yan et al., 2010).

On the Qt-F-L ternary diagram (Fig. 10B), all sandstone samples plot in the recycled orogen provenance domain (Garzanti, 2016). On the Qp-Lv-Ls ternary diagram (Fig. 10C), sandstone samples from the Lower member of the Chishan Formation plot in the collision suture and fold-thrust belt sources domain, and those from the Upper member of the Chishan Formation fall in the arc orogen provenance domain (Dickinson, 1985).

Detrital zircon provenance

Detrital zircon age groups of Early Cretaceous, Triassic, Early Paleozoic, Neoproterzoic, Paleoproterzoic−Archean were recognized and identified for the studied samples (Fig. 11A; Table S4). These age clusters are consistent with the Yanshanian, Indosinian, Caledonian, Jinningian, Luliangian, and Wutai orogenies that occurred in

China (He et al., 2013), implying a mixed source pattern. These age populations overlap with the age spectra of the Sulu orogenic belt, Zhangbaling Uplift, and Yangtze and Cathaysian blocks on the KDE diagrams (Fig. 11A). Six sandstone samples from the Chishan Formation have their main age peaks at 126−142 Ma and 595−985 Ma (Fig. 11A), which predominantly occurred in the Sulu orogenic belt and Zhangbaling Uplift. The sandstone samples from the Lower Chishan Formation have low percentages of age peaks of 1825−2000 Ma (8%) and 2400−2560 Ma (8.7%), and high percentages of 595−985 Ma age population (43%) (Fig. 11A; Table S5).

However, a marked change in the proportions of age clusters is observed from analysis of deposits of the Upper Chishan Formation. The sandstone samples from this unit have distinctive age peaks at 1825−2000 Ma (16.2%) and 2400−2560 Ma (19.2%), with a significant decrease in age groups of 595–985 Ma (26.6%) (Fig. 11A; Table S5), indicating a notable variation in provenance.

DISCUSSION

Cretaceous plateau cryosphere

Anchor ice and ice floe were generated in water of oases in a hyper-arid plateau desert in winter when supercooling temperatures (−12℃) and strong freezing winds occurred (Wu and Rodríguez-López, 2021). Such ice can erode and transport interdune mud intraclasts under the effect of wind shear, water-level fluctuation, and periodic freezing and melting. The processes lead to the formation of ice-rafted intraclasts in the oases sediments. Our data from sedimentary lithofacies indicate the occurrence of Upper Cretaceous ice-rafted debris in desert oasis deposits of the East Asian continental

353 margin, implying that Subei desert basin reached a paleoelevation where altitudinal
354 cryospheric processes were possible, similar to those occurring in the Quaternary
355 Badain Jaran Desert oases from China (Wu and Rodríguez-López, 2021).

356 The Cretaceous was a major supergreenhouse period of Earth history that
357 witnessed extreme warmth (3−10 ℃ warmer than today) (Skelton et al., 2003). Hitherto,
358 it has been widely suggested that there was no continental ice during this greenhouse
359 period (Huber et al., 2002; Miller et al., 2005; Forster et al., 2007). However, in recent
360 years, increasing evidence has been put forward to indicate that global cooling events
361 or cryospheric conditions occurred in the Atlantic, Antarctica, Canada, Europe,
362 Australia, Alaska, and China during the Cretaceous period (e.g., Frakes et al., 1995;
363 Macquaker and Keller, 2005; Miller et al., 2005; Bowman et al., 2013; Linnert et al.,
364 2014; Rodríguez-López et al., 2016; Rogov et al., 2017; Grasby et al., 2017; Niezgodzki
365 et al., 2019; Galloway et al., 2020; Alley et al., 2020; Cavalheiro et al., 2021; Wu et al.,
366 2022). The proposal of a Cretaceous cryosphere is mainly based on the recognition of
367 ice-rafted dropstones and diamictites (Frakes and Francis, 1988; Wang et al., 1996;
368 Price, 1999; Cheng et al., 2002; Alley and Frakes, 2003; Simmons, 2012; Hore et al.,
369 2015; Jeans and Platten, 2021; Wu and Rodríguez-López, 2021), glendonites (Herrle et
370 al., 2015; Grasby et al., 2017; Vickers et al., 2019; Rogov et al., 2021), permafrost
371 wedges (Rodríguez-López et al., 2022; Wang et al., 2023), and ultra-depleted hydrogen
372 and oxygen isotopes (Bornemann et al., 2008; Yang et al., 2013; Nelson et al., 2022).
373 Recently, a comparison analysis of major climatic drivers argues for the link between
374 significant short-term Cretaceous sea-level change and glacio-eustasy (Ray et al., 2019).

Collectively, these studies imply the possible occurrence of a Cretaceous global glaciation environment.

In detail, evidence occurs as Valanginian−Hauterivian glacial debris flows and sand wedges in the Ordos Basin (Cheng et al., 2002; Wang et al., 2023), early Aptian extremely negative $\delta^{18}O$ values of hydrothermal zircon in an A-type granite at Baerzhe in northeastern China (Yang et al., 2013), Cenomanian−Turonian ice-rafted debris in the Songliao, Chuxiong and Simao basins (Wang et al., 1996; Wu and Rodríguez-López, 2021), and Campanian striated cobbles in the Xinjiang Basin (Jiao et al., 2020). Combined with Santonian to Campanian glaciations in plateau desert oases of the South China coastal mountains, such evidence indicates the occurrence of a Cretaceous plateau cryosphere in China, which correlates with the appearance of global significant short-term eustatic variations, glendonites and dropstones (Ray et al., 2019; Wu et al., 2022).

In addition, following especially warm climate conditions at the boundary of the Cenomanian/Turonian, long-term global cooling was underway by at least the late Turonian and this trend intensified during the Campanian (Pucéat et al., 2003; Friedrich et al., 2012; Linnert et al., 2014). The Santonian to Campanian Chishan Formation spans this event of cooling intensification. This leads us to propose that cryospheric processes in the Subei desert record the secular cooling in the Late Cretaceous.

Late Cretaceous East Asian marginal plateau

The Cathaysian coastal mountains were first proposed by Chen (1997) based on analyses of thick-bedded molasse accumulations and paleontological records. An

increasing body of evidence from basin provenance analyses (Tan et al., 2020; Chen et al., 2021), thermochronology (Li and Zou, 2017), carbonate clumped isotope paleothermometry (Zhang et al., 2016), and paleo-topographic modeling (Liu et al., 2020; Zhang et al., 2021) suggests that a coastal mountain range with a paleoelevation of ≥2000 m existed along the South China continental margin from the Jiaolai basin to Hainan island during the Late Jurassic to Cretaceous (Fig. 1A).

The provenance signature of the lower fluvial to upper aeolian strata from the Chishan Formation records a change in sand composition and detrital zircon age. Although litho-quartzose sands overall, the Upper Chishan Formation displays a substantial increase in component volcanic lithic grains, whereas the lithic grains from the Lower Chishan Formation are mostly of sedimentary origin (Fig. 10C). Furthermore, the detrital zircon U-Pb ages from the Lower unit are dominated by Mesozoic and Neoproterozoic ages, whereas zircons older than 1.6 Ga occur more frequently in the Upper Chishan Formation (Fig. 11A). The Paleoproterzoic−Archean zircon grains are in agreement with the ages of the dominant stages of crustal growth in South China (Li et al., 1992). This may imply that the Paleoproterozoic to Archean basement of the South China Block was a source area for the aeolian Upper unit. Given evidence of the south-easterly-directed paleocurrents preserved in the water-lain sediments (Fig. 2), the Sulu orogenic belt to the north and the Zhangbaling Uplift to the west were likely the major sediment sources for the Subei basin during deposition of the Lower Chishan Formation.

To evaluate the relationship of Chishan Formation sands with basement sources,

plots of MDS (Figs. 11B and 11C) and CPD (Fig. 12) compare our data with local basement sources based on previously published detrital zircon data. The Lower Chishan Formation has a similar contribution to Sulu Orogen and Zhangbaling Uplift, whereas the Upper Chishan Formation displays an increase of similarity with samples from the Yangtze Block. The sandstone modal compositions suggest a change in tectonic setting from collision suture and fold-thrust belt sources, to an arc-orogen source (Fig. 10C). Thus, it is suggested that the clastic sediments from the Chishan Formation should be mostly recycled from the Sulu orogenic belt and Zhangbaling Uplift, together with Early Cretaceous magmatic rocks developed in them. In addition, exposure and erosion of the pre-Cretaceous basement of the Yangtze Block caused by the collision between the Okhotomorsk Block and the South China Block along the East Asian margin (Yang, 2013; Zhang et al., 2016) supplied a distinct sediment source for the Upper section of this formation. Meanwhile, the synchronous cryospheric processes in the Subei desert indicate that this orogeny enabled plateau deserts to reach altitudes at which seasonal ice developed. A modern example of a high-altitude aeolian–permafrost system at Qiongkuai Lebashi Lake in the western Himalayas of China showcases a frozen desert oases at 3,308 m above sea level (Rodríguez-López et al., 2022). A combination of global cooling events from the late Turonian to Maastrichtian and the high topography of the coastal mountains may have resulted in the development similar glacial activity in the Cretaceous succession that is the focus of this study.

In combination with characterization of sedimentary facies (Yue et al., 1997; Yue and Ding, 1999), a two-stage evolution model presenting the paleogeography of the

East Asian continental margin is proposed (Fig. 13). During the early deposition stage of the Chishan Formation, subduction of the Izanagi Plate into Eurasia led to the formation of back-arc fault basins. The rapid exhumation of the Sulu orogenic belt and Zhangbaling Uplift provided the main sources for the Subei basin (Fig. 13A). From west to east, alluvial, fluvial and lacustrine deposits were developed in the basin (Fig. 13B). During the late deposition stage of the Chishan Formation, aeolian dune and interdune facies associations were accumulated during an arid climate (Fig. 13D). At this time, the Subei basin received significant clastic sediments from the pre-Cretaceous basement of the Yangtze Block. The change in provenance and paleogeography is possibly connected with the tectonic dynamics in the region (Yang, 2013, Tan et al., 2020) whereby a collision between the Okhotomorsk Block and the East Asian continent occurred along the East Asian continental margin (Fig. 13C).

CONCLUSIONS

We characterize the presence of ice-rafted dropstones and diamictites from the Upper Cretaceous Chishan Formation of the Subei Basin, and use paleocurrent, petrography and detrital zircon U-Pb geochronogy data to reveal the provenance. Our results suggest that the clastic sediments from the Chishan Formation were mostly recycled from the Sulu orogenic belt and Zhangbaling Uplift. Furthermore, the pre-Cretaceous basement of the Yangtze Block provided a significant detritus for aeolian deposits in the Lower Chishan Formation. The change in provenance is related to the collision between the Okhotomorsk Block and the South China Block along the East Asian margin leading to the occurrence of the South China coastal mountains,

generating an arid-climate, high-altitude basin region. This orogeny enabled plateau deserts to reach altitudes at which ice-related deposits developed, coupled with global cooling from the late Turonian to Maastrichtian, as recorded in the Subei desert basin. Our results for the Late Cretaceous paleoclimate and paleogeography at the East Asian continental margin have implications for the developments of an active Cretaceous plateau cryosphere associated with lithosphere dynamics.

ACKNOWLEDGMENTS

We thank Donghong Li for his assistance in the field work, and an anonymous reviewer, Charlotte L. Priddy and associate editor for their helpful comments, which have significantly improved the manuscript. The study was supported by the National Key Research and Development Program of China (2023YFC2906605) and the Scientific Research Fund of the China Central Non-Commercial Institute (KK2005 and KK2322).

REFERENCES CITED

Allen, J.P., Fielding, R.F., Gibling, M.R., and Rygel, M.C., 2014, Recognizing products of paleoclimate fluctuation in the fluvial stratigraphic record: an example from Pensylvanian to lower permian of Cape Breton Island, Nova Scotia: Sedimentology, v. 61, p. 1332–1381, https://doi.org/10.1111/sed.12102.

Alley, N.F., and Frakes, L.A., 2003, First known Cretaceous glaciation: Livingston tillite member of the Cadna-owie formation, South Australia: Australian Journal of Earth Sciences, v. 50, p. 139–144, https://doi.org/10.1046/j.1440-0952.2003.00984.x.

485 Alley, N.F., Hore, S.B., and Frakes, L.A., 2020, Glaciations at high-latitude Southern
486 Australia during the Early Cretaceous: Australian Journal of Earth Sciences, v. 67,
487 p. 1045–1095, https://doi.org/10.1080/08120099.2019.1590457.
488 Basilici, G., Colombera, L., Soares, M.V.T., Arévalo, O.J., Mountney, N.P., Lorenzoni,
489 P., Filho, C.R.S., Mesquita, Á.F., and Janočko, J., 2022, Variations from dry to
490 aquic conditions in Vertisols (Esplugafreda Formation, Eastern Pyrenees, Spain):
491 Implications for late Paleocene climate change: Palaeogeography,
492 Palaeoclimatology, Palaeoecology, v. 595, 110972,
493 https://doi.org/10.1016/j.palaeo.2022.110972.
494 Benvenuti, M., 2003, Facies analysis and tectonic significance of lacustrine fan-deltaic
495 successions in the pliocene-pleistocene Mugello basin, Central Italy: Sedimentary
496 Geology, v. 157, p. 197–234, https://doi.org/10.1016/S0037-0738(02)00234-8.
497 BGMRJ, Bureau of Geology, Mineral Resources of Jiangsu Province, 1997, Rock
498 Stratigraphy in Jiangsu Province: Wuhan, China University of Geosciences Press,
499 288 p.
500 Bornemann, A., Norris, R.D., Friedrich, O., Beckmann, B., Schouten, S., Damsté, J.S.S.,
501 Vogel, J., Hofmann, P., and Wagner, T., 2008, Isotopic evidence for glaciation
502 during the Cretaceous supergreenhouse: Science, v. 319, p. 189–192,
503 https://doi.org/10.1126/science.11487.
504 Bowman, V.C., Francis, J.E., and Riding, J.B., 2013, Late Cretaceous winter sea ice in
505 Antarctica: Geology, v. 41, p. 1227–1230, https://doi.org/10.1130/G34891.1.
506 Cao, S., Zhang, L., Mountney, N.P., Ma, J., Hao, M. and Wang, C., 2023a, Ultra-long-

distance transport of aeolian sand: The provenance of an intermontane desert, south-east China: Sedimentology, v. 70, p. 2108–2126, https://doi.org/10.1111/sed.13106.

Cao, S., Ma, J., and Wang C.S., 2023b, The sedimentological characteristics of the intermontane desert system in the Jurong Basin, South China and its relationship with the Late Cretaceous hot climate: Palaeogeography, Palaeoclimatology, Palaeoecology, v. 623, 111618, https://doi.org/10.1016/j.palaeo.2023.111618.

Cavalheiro, L., Wagner, T., Steinig, S., Bottini, C., Dummann, W., Esegbue, O., Gambacorta, G., Giraldo-Gómez, V., Farnsworth, A., Flögel, S., Hofmann, P., Lunt, D.J., Rethemeyer, J., Torricelli, S., and Erba, E., 2021, Impact of global cooling on Early Cretaceous high pCO_2 world during the Weissert Event: Nature Communications, v. 12, 5411, https://doi.org/10.1038/s41467-021-25706-0.

Charles, N., Chen, Y., Augier, R., Gumiaux, C., Lin, W., Faure, M., Monie, P., Choulet, F., Wu, F.Y., Zhu, R.X., and Wang, Q.C., 2011, Palaeomagnetic constraints from granodioritic plutons (Jiaodong Peninsula): New insights on Late Mesozoic continental extension in Eastern Asia: Phys. Physics of the Earth and Planetary Interiors, v. 187, p. 276–291, https://doi.org/10.1016/j.pepi.2011.05.006.

Chen, A.D., 2010, Tectonic features of the Subei Basin and the forming mechanism of its dustpan-shaped fault depression: Oil & Gas Geology, v. 31, p. 140–150, https://doi.org/10.11743/ogg20100202.

Chen, M., Zheng, J.P., Sun, M., and Zhao, J.H., 2013, Mid-Neoproterozoic crustal evolution of the northeastern Yangtze Block: Evidence from the felsic-gneiss

529 xenoliths hosted, in the Donghai Cenozoic basalts: Journal of Asian Earth Sciences,
530 v. 66, p. 108–122, https://doi.org/10.1016/j.jseaes.2012.12.032.
531 Chen, P.J., 1997, Coastal mountains of SE China, desertization and saliniferous lakes
532 of central China during the Late Cretaceous: Journal of stratigraphy, v. 21, p. 203–
533 213, https://doi.org/CNKI:SUN:DCXZ.0.1997-03-003.
534 Chen, Y., Meng, J., Liu, H., Wang, C.S., Tang, M., Liu, T., and Zhao, Y.N., 2021,
535 Detrital zircons record the evolution of the Cathaysian Coastal Mountains along
536 the South China margin: Basin Research, 34, 688–701,
537 https://doi.org/10.1111/bre.12636.
538 Cheng, S.T., Li, Z.D., Huang, Y.Q., Ge, L., and Liu, X., 2002, Discovery and its genetic
539 evidence of Early Cretaceous glacial debris flow in the northeast margin of Ordos:
540 Geol. Sci. Technol. In. v. 21, p. 36–40,
541 https://doi.org/10.1080/12265080208422884.
542 Cheng, S.T., Li, Z.D., Huang, Y.Q., Ge, L., and Liu, X., 2002, Discovery and its genetic
543 evidences of Early Cretaceous glacial debris flow in the northeast margin of Ordos:
544 Geological Science and Technology Information, v. 21, p. 36–40,
545 https://doi.org/10.3969/j.issn.1000-7849.2002.02.007.
546 Clemmensen, L.B., 1989, Preservation of interdraa and plinth deposits by the lateral
547 migration of large linear draas (Lower Permian Yellow Sands, northeast England):
548 Sedimentary Geology, v. 65, p. 139–151, https://doi.org/10.1016/0037-
549 0738(89)90011-0.
550 Cosgrove, G.I.E., Colombera, L., and Mountney, N.P., 2022, Eolian stratigraphic record

551 of environmental change through geological time: Geology, v. 150, p. 289–294,
552 https://doi.org/10.1130/G49474.1.
553 Darby, B.J., and Gehrels, G., 2006, Detrital zircon reference for the North China block:
554 Journal of Asian Earth Sciences, v. 26, p. 637–648,
555 https://doi.org/10.1016/j.jseaes.2004.12.005.
556 Dickinson, W.R., 1985, Interpreting provenance relations from detrital modes of
557 sandstones, in Zuffa, G.G., ed., Provenance of arenites, NATO ASI Series, v. 148,
558 p. 333–361, https://doi.org/10.1007/978-94-017-2809-6_15.
559 Dickinson, W.R., and Suczek, C., 1979, Plate tectonics and sandstone composition:
560 AAPG Bulletin, v. 63, p. 2164–2182, https://doi.org/10.1306/2F9188FB-16CE-
561 11D7-8645000102C1865D.
562 Diwu, C., Sun, Y., Yuan, H., Wang, H., Zhong, X., and Liu, X., 2008, U-Pb ages and Hf
563 isotopes for detrital zircons from quartzite in the Paleoproterozoic Songshan
564 Group on the southwestern margin of the North China Craton: Chinese Science
565 Bulletin, v. 53, p. 2828–2839, https://doi.org/10.1007/s11434-008-0342-1.
566 Du, L., Yang, C., Wang, W., Ren, L., Wan, Y., Song, H., Gao, L., Geng, Y., and Hou, K.,
567 2012, Provenance of the Paleoproterozoic Hutuo Group basal conglomerates and
568 Neoarchean crustal growth in the Wutai Mountains, North China Craton: Evidence
569 from granite and quartzite pebble zircon U-Pb ages and Hf isotopes: Science China
570 Earth Sciences, v. 55, p. 1796–1814, https://doi.org/10.1007/s11430-012-4407-2.
571 Duan, L., Meng, Q.R., Wu, G.L., Ma, S.X., and Li, L., 2012, Detrital zircon evidence
572 for the linkage of the South China block with Gondwanaland in early Palaeozoic

573 time: Geological Magazine, v. 149, p. 1124–1131,
574 https://doi:10.1017/S0016756812000404.
575 Forster, A., Schouten, S., Baas, M., and Sinninghe Damsté, J.S., 2007, Mid-Cretaceous
576 (Albian-Santonian) sea surface temperature record of the tropical Atlantic Ocean:
577 Geology, v. 35, p. 919–922, https://doi.org/10.1130/G23874A.1.
578 Frakes, L.A., Alley, N.E., and Deynoux, M., 1995, Early Cretaceous ice rafting and
579 climate zonation in Australia. International Geology Review, v. 37, p. 567–583,
580 https://doi.org/10.1080/00206819509465419.
581 Frakes, L.A., and Francis, J.E., 1988, A guide to Phanerozoic cold polat climates from
582 high-latitude ice-rafting in the Cretaceous: Nature, v. 333, p. 547–549,
583 https://doi.org/10.1038/333547a0.
584 Friedrich, O., Norris, R.D., and Erbacher, J., 2012, Evolution of middle to Late
585 Cretaceous oceans – A 55 m.y. record of Earth's temperature and carbon cycle:
586 Geology, v. 40, p. 471 107–110, https://doi.org/10.1130/G32701.1.
587 Frisch, K., Voigt, S., Voigt, T., Hellwig, A., Verestek, V., and Weber, Y., 2019, Extreme
588 aridity prior to lake expansion deciphered from facies evolution in the Miocene Ili
589 Basin, South-East Kazakhstan: Sedimentology, v. 66, p. 1716–1745,
590 https://doi.org/10.1111/sed.12556.
591 Galloway, J.M., Vickers, M.L,, Price, G.D., Poulton, T., Grasby, SE., Hadlari, T.,
592 Beauchamp B., and Sulphur K., 2020, Finding the VOICE: organic carbon isotope
593 chemostratigraphy of the Late Jurassic–Early Cretaceous of Arctic Canada:
594 Geological Magazine, v. 157, p. 1643–1657, https://doi.org/10.1017/

595 S0016756819001316.
596 Garzanti, E., 2016, From static to dynamic provenance analysis—Sedimentary
597 petrology upgraded: Sedimentary Geology, v. 336, p. 3–13,
598 https://doi.org/10.1016/j.sedgeo.2015.07.010.
599 Grasby, S.E., McCune, G.E., Beauchamp, B., and Galloway, J.M., 2017, Lower
600 Cretaceous cold snaps led to widespread glendonite occurrences in the Sverdrup
601 Basin, Canadian High Arctic: Geological Society of America Bulletin, v. 129, p.
602 771–787, https://doi.org/10.1130/B31600.1.
603 Hasegawa, H., Tada, R., Jiang, X., Suganuma, Y., Imsamut, S., Charusiri, S., Ichinnorov,
604 N., and Khand, Y., 2012, Drastic shrinking of the Hadley circulation during the
605 mid-Cretaceous supergreenhouse: Climate of the Past, v. 7, p. 119–151,
606 https://doi.org/10.5194/cp-8-1323-2012.
607 He, M., Zheng, H., and Clift, P.D., 2013, Zircon U−Pb geochronology and Hf isotope
608 data from the Yangtze River sands: Implications for major magmatic events and
609 crustal evolution in Central China: Chemical Geology, v. 360, p. 186–203,
610 https://doi.org/10.1016/j. chemgeo.2013.10.020.
611 Huang, J., Zheng, Y.F., Zhao, Z.F., Wu, Y.B., Zhou, J.B., and Liu, X.M., 2006, Melting
612 of subducted continent: element and isotopic evidence for a genetic relationship
613 between Neoproterozoic and Mesozoic granitoids in the Sulu orogen: Chemical
614 Geology v. 229, p. 227–256, https://doi.org/10.1016/j.chemgeo.2005.11.007.
615 Huber, B.T., Norris, R.D., and MacLeod, K.G., 2002, Deep-sea paleotemperature
616 record of extreme warmth during the Cretaceous: Geology, v. 30, p. 123–126,

https://doi.org/10.1130/0091-7613.

Hunter, R.E., 1977, Basic types of stratification in small eolian dunes: Sedimentology, v. 24, p. 361–387, https://doi.org/10.1111/j.1365-3091.1977.tb00128.x.

Ingersoll, R.V., Bullard, T.F., Ford, R.L., Grimm, J.P., Pickle, J.D., and Sares, S.W., 1984, The effect of grain-size on detrital modes: a test of the Gazzi-Dickinson point-counting method: Journal of Sedimentary Research, v. 54, p. 103–116, https://doi.org/10.1306/212F83B9-2B24-11D7-8648000102C1865D.

Jeans, C. V., and Platten, I. M., 2021, The erratic rocks of the Upper Cretaceous Chalk of England: how did they get there, ice transport or other means?: Acta Geological Polonica, v. 71, p. 287–304, https://doi.org/10.24425/agp.2020.134555.

Jiang, X.S., Pan, Z.X., Xu, J.S., Li, X.Y., Xie, G.G., and Xiao, Z.J., 2008, Late Cretaceous Aeolian dunes and reconstruction of palaeowind belts of the Xinjiang Basin, Jiangxi Province, China: Palaeogeography, Palaeoclimatology, Palaeoecology, v. 257, p. 58–66, https://doi.org/10.1016/j.palaeo.2007.09.012.

Jiao, H., Wu, C., Rodríguez-López, J.P., Sun, X., and Yi, H., 2020, Late Cretaceous plateau deserts in the South China Block, and quaternary analogues; sedimentology, dune reconstruction and wind-water interactions: Marine and Petroleum Geology, v. 120, 104504, https://doi.org/10.1016/j.marpetgeo.2020.104504.

Katsube, A., Hayasaka, Y., Santosh, M., Li, S.Z., and Terada, K., 2009, SHRIMP zircon U–Pb ages of eclogite and orthogneiss from Sulu ultrahigh-pressure zone in Yangkou area, eastern China: Gondwana Research, v. 15, p. 168–177,

https://doi.org/10.1016/j.gr.2008.08.002.

Kocurek, G., 1981, Significance of interdune deposits and bounding surfaces in aeolian dune sands: Sedimentology, v. 28, p. 753–780, https://doi.org/10.1111/j.1365-3091.1981.tb01941.x.

Kocurek, G., 1991, Interpretation of ancient eolian sand dunes: Annual Review of Earth and Planetary Sciences, v. 19, p. 43–75, https://doi.org/10.1146/annurev.ea.19.050191.000355.

Lacotte, V.J.P.H., and Mountney, N.P., 2022, A classification scheme for sedimentary architectures arising from aeolian-fluvial system interactions: Permian examples from southeast Utah, USA: Aeolian Research, v. 58, 100815, https://doi.org/10.1016/j.aeolia.2022.100815.

Lan, T.G., Fan, H.R., Santosh, M., Hu, F.F., Yang, K.F., Yang, Y.H., and Liu, Y.S., 2011, Geochemistry and Sr–Nd–Pb–Hf isotopes of the Mesozoic Dadian alkaline intrusive complex in the Sulu orogenic belt, eastern China: implications for crust–mantle interaction: Chemical Geology, v. 285, p. 97–114, https://doi.org/10.1016/j.chemgeo.2011.03.013.

Le Heron, D.P., Tofaif, S., Vandyk, T., and Ali, D.O., 2017, A diamictite dichotomy: glacial conveyor belts and olistostromes in the Neoproterozoic of Death Valley, California, USA: Geology, v. 45, p. 31–34, https://doi.org/10.1130/G38460.1.

Li, H., Xu, Y., Huang, X., He, B., Luo, Z. and Yan, B., 2008a, Activation of northern margin of the North China Craton in Late Paleozoic: Evidence from U-Pb dating and Hf isotopes of detrital zircons from the Upper Carboniferous Taiyuan

661 Formation in the Ningwu-Jingle basin: Chinese Science Bulletin, v. 54, p. 677–
662 686, https://doi.org/10.1007/s11434-008-0444-9.
663 Li, H.B., Jia, D., Wu, L., Zhang, Y., Yin, H.W., Wei, G.Q. and Li, B.L., 2013a, Detrital
664 zircon provenance of the Lower Yangtze foreland basin deposits: constraints on
665 the evolution of the early Palaeozoic Wuyi–Yunkai orogenic belt in South China:
666 Geological Magazine, v. 150, p. 959–974,
667 https://doi:10.1017/S0016756812000969.
668 Li, H.Y., Chen, R.X., Zheng, Y.F., and Hu, Z.C., 2016, The crust-mantle interaction in
669 continental subduction channels: zircon evidence from orogenic peridotite in the
670 Sulu orogen: Journal of Geophysical Research: Solid Earth, v. 121, p. 687–712,
671 https://doi.org/10.1002/2015JB012231.
672 Li, H.Y., He, B., Xu, Y.G., and Huang, X.L., 2010, U-Pb and Hf isotope analyses of
673 detrital zircons from Late Paleozoic sediments: Insights into interactions of the
674 North China Craton with surrounding plates: Journal of Asian Earth Sciences, v.
675 39, p. 335–346, https://doi.org/10.1016/j.jseaes.2010.05.002.
676 Li, H.Y., Xu, Y.G., Liu, Y.M., Huang, X.L., and He, B., 2013b, Detrital zircons reveal
677 no Jurassic plateau in the eastern North China Craton: Gondwana Research, v. 24,
678 p. 622–634, https://doi.org/10.1016/j.gr.2012.12.007.
679 Li, L.M., Sun, M., Wang, Y., Xing, G., Zhao, G., He, Y., He, K., and Zhang, A., 2011,
680 U–Pb and Hf isotopic study of detrital zircons from the meta-sedimentary rocks in
681 central Jiangxi Province, South China: implications for the Neoproterozoic
682 tectonic evolution of South China Block: Journal of Asian Earth Sciences, v. 41,

683 p. 44–55, https://doi.org/10.1016/j.jseaes.2010.12.004.
684 Li, Q., Liu, S., Wang, Z., Chu, Z., Song, B., Wang, Y., and Wang, T., 2008b, Contrasting
685 provenance of Late Archean metasedimentary rocks from the Wutai Complex,
686 North China Craton: detrital zircon U–Pb, whole-rock Sm–Nd isotopic, and
687 geochemical data: International Journal of Earth Sciences, v. 97, p. 443–458,
688 https://doi.org/10.1007/s00531-007-0170-6.
689 Li, X. M., and Zou, H., 2017, Late Cretaceous-Cenozoic exhumation of the
690 southeastern margin of Coastal Mountains, SE China, revealed by fission-track
691 thermochronology: Implications for the topographic evolution: Solid Earth
692 Sciences, v. 2, p. 79–88, https://doi.org/10.1016/j.sesci.2017.02.001.
693 Li, X.H., Li, Z.X., He, B., Li, W.X., Li, Q.L., Gao, Y., and Wang, X.C., 2012, The Early
694 Permian active continental margin and crustal growth of the Cathaysia Block: in
695 situ U–Pb, Lu–Hf and O isotope analyses of detrital zircons: Chemical Geology,
696 v. 328, p. 195–207, https://doi.org/10.1016/j.chemgeo.2011.10.027.
697 Li, X.H., Zhao, Z.H., Gui, X.T., and Yu, J.S., 1992, Sm-Nd isotopic and zircon U-Pb
698 constraints on the age of formation of the Precambrian crust in Southeast China:
699 Chinese Journal of Geochemstry, v. 11, p. 111–120,
700 https://doi.org/10.1007/BF02871998.
701 Li, Y.X., Yan, J., Song, C.Z., Li, C., Yang, Q.L., and Li, Z.S., 2021, Petrogenesis of late
702 Mesozoic granitoids from the southern segment of the Tan–Lu Fault, eastern China:
703 implications for the tectonic affinity of the Zhangbaling Uplift: International
704 Geology Review, v. 63, p. 453–475,

https://doi.org/10.1080/00206814.2020.1716401.

Li, Z., Chen, B., Wei, C., Wang, C., and Han, W., 2015, Provenance and tectonic setting of the Paleoproterozoic metasedimentary rocks from the Liaohe Group, Jiao-Liao-Ji Belt, North China Craton: Insights from detrital zircon U–Pb geochronology, whole-rock Sm–Nd isotopes, and geochemistry: Journal of Asian Earth Sciences, v. 111, p. 711–732, https://doi.org/10.1016/j.jseaes.2015.06.003.

Linnert, C., Robinson, S. A., Lees, J.A., Bown, P.R., Perez-Rodriguez, I., Petrizzo, M.R., Falzoni, F., Littler, K., Arz, J.A., Russell, E.E., 2014, Evidence for global cooling in the Late Cretaceous: Nature Communications, v. 5, 4194, https://doi.org/10.1038/ncomms5194.

Liou, J.G., Tsujimori, T., Chu, W., Zhang, R.Y., and Wooden, J.L., 2006, Protolith and metamorphic ages of the Haiyangsuo Complex, eastern China: a non-UHP exotic tectonic slab in the Sulu ultrahigh-pressure terrane: Mineralogy and Petrology, v. 88, p. 207–226, https://doi.org/10.1007/s00710-006-0156-2.

Liu, F.L., Xu, Z.Q., Liou, J.G., and Song, B., 2004, SHRIMP U-Pb ages of ultrahigh-pressure and retrograde metamorphism of gneisses, south-western Sulu terrane, eastern China: Journal of Metamorphic Geology, v. 22, p. 315–326, https://doi.org/10.1111/j.1525-1314.2004.00516.x.

Liu, J.H., Liu, F.L., Ding, Z.J., Yang, H., Liu, C.H., Liu, P.H., Xiao, L.L., Zhao, L., and Geng, J.Z., 2013, U–Pb dating and Hf isotope study of detrital zircons from the Zhifu Group, Jiaobei Terrane, North China Craton: provenance and implications for Precambrian crustal growth and recycling: Precambrian Research, v. 235, p.

230–250, https://doi.org/10.1016/j.precamres.2013.06.014.

Liu, S., Hu, R.Z., Gao, S., Feng, C.X., Qi, Y.Q., Wang, T., Feng, G.Y., and Coulson, I.M., 2008a, U–Pb zircon age, geochemical and Sr–Nd–Pb–Hf isotopic constraints on age and origin of alkaline intrusions and associated mafic dikes from Sulu orogenic belt, Eastern China: Lithos, v. 106, p. 365–379, https://doi.org/10.1016/j.lithos.2008.09.004.

Liu, S., Hu, R.Z., Gao, S., Feng, C.X., Zhong, H., Qi, Y.Q., Wang, T., Feng, G.Y., and Yang, Y.H., 2011, U–Pb zircon ages, geochemical and Sr–Nd–Pb isotopic constraints on the dating and origin of intrusive complexes in the Sulu orogen, eastern China: International Geology Review, v. 53, p. 61–83, https://doi.org/10.1080/00206810902900319.

Liu, X.M., Gao, S., Diwu, C.R., and Ling, W.L., 2008b, Precambrian crustal growth of Yangtze craton as revealed by detrital zircon studies: American Journal of Science, v. 308, p. 421–468, https://doi.org/10.2475/04.2008.02.

Liu, Z., Dai, L. M., Li, S.Z., Li, Z.H., Ding, X.S., Bukhari, S.W.H., and Somerville, I., 2020, Earth's surface responses during geodynamic evolution: Numerical insight from the southern East China Sea Continental Shelf Basin, West Pacific: Gondwana Research, v. 102, p. 167–179, https://doi.org/10.1016/j.gr.2020.12.011.

Macquaker, J.H.S., and Keller, M.A., 2005, Mudstone sedimentation at high latitudes: ice as a transport medium for mud and supplier of nutrients: Journal of Sedimentary Research, v. 75, p. 696–709, https://doi.org/10.2110/jsr.2005.056.

Miall, A., 1996, Geology of fluvial deposits: Berlin, SpringerVerlag, 582 p.

749 Miall, A.D., 1977, A review of the braided-river depositional environment: Earth-
750 Science Reviews, v. 13, p. 1–62, https://doi.org/10.1016/0012-8252(77)90055-1.
751 Miller, K.G., Wright, J.D., and Browning, J.V., 2005, Visions of ice sheets in a
752 greenhouse world: Marine Geology, v. 217, p. 215–231,
753 https://doi.org/10.1016/j.margeo.2005.02.007.
754 Mountney, N.P., and Thompson, D.B., 2002, Stratigraphic evolution and preservation
755 of aeolian dune and damp/wet interdune strata: an example from the Triassic
756 Helsby Sandstone Formation, Cheshire Basin, UK: Sedimentology 49, 805–833,
757 https://doi.org/10.1046/j.1365-3091.2002.00472.x.
758 Nelson, D. A., Cottle, J. M., Bindeman, I. N., and Camacho, A., 2022, Ultra-depleted
759 hydrogen isotopes in hydrated glass record Late Cretaceous glaciation in
760 Antarctica: Nature Communications, v. 13, 5209, https://doi.org/10.1038/s41467-
761 022-32736-9.
762 Niezgodzki, I., Tyszka, J., Knorr, G., and Lohmann, G., 2019, Was the Arctic Ocean ice
763 free during the latest Cretaceous? The role of CO2 and gateway configurations:
764 Global and Planetary Change, v. 177, p. 201–212,
765 https://doi.org/10.1016/j.gloplacha.2019.03.011.
766 Niu, M.L., Cai, Q.R., Wu, Q., Yuan, X.Y., Sun, Y., Li, X.C., Li, C., Zhu, G., Li, Z.S.,
767 and Zhang, S., 2020, Neoproterozoic Crustal Reworking and Growth in the
768 Zhangbaling Uplift, Tan–Lu Fault Zone: Evidence from the Feidong Complex and
769 Zhangbaling Group: Acta Geologica Sinica (English Edition), v. 94, p. 1921–1939,
770 https://doi.org/10.1111/1755-6724.14604.

771 Niu, M.L., Zhu, G., Xie, C.L., Liu, X.M., Cao, Y., and Xie, W.X., 2008, LA-ICP-MS
772 zircon U–Pb ages of the granites from the southern segment of the Zhangbaling
773 uplift along the Tan–Lu Fault Zone and their tectonic significances: Acta
774 Petrologica Sinica, v. 24, p. 1839–1847.
775 Price, G.D., 1999, The evidence and implications of Polar Ice during the Mesozoic:
776 Earth-Science Reviews, v. 48, p. 183–210, https://doi.org/10.1016/S0012-
777 8252(99)00048-3.
778 Pucéat, E., Lecuyer, C., Sheppard, S. M.F., Dromart, G., Reboulet, S., and Grandjean,
779 P., 2003, Thermal evolution of Cretaceous Tethyan marine waters inferred from
780 oxygen isotope composition of fish tooth enamels: Paleoceanography and
781 Paleoclimatology, v. 18, 1029, https://doi.org/10.1029/2002PA000823.
782 Ray, D.C., van Buchem, F.S.P., Baines, G., Davies, A., Gréselle, B., Simmons, M.D.,
783 and Robson, C., 2019, The magnitude and cause of short-term eustatic Cretaceous
784 sea-level change: a synthesis: Earth-Science Reviews, v. 197, 102901,
785 https://doi.org/10.1016/j.earscirev.2019.102901.
786 Retallack, G.J., 1994, The environmental factor approach to the interpretation of
787 paleosols: SSSA Special Publication, v.33, p. 31–64,
788 https://doi.org/10.2136/sssaspecpub33.c3.
789 Rodríguez-López, J.P., Clemmensen, L.B., Lancaster, N., Mountney, N.P., and Veiga,
790 G.D., 2014, Archean to recent aeolian sand systems and their sedimentary record:
791 current understanding and future prospects: Sedimentology, v. 61, p. 1487–1534,
792 https://doi.org/10.1111/sed.12123.

793 Rodríguez-López, J.P., Liesa, C.L., Pardo, G., Meléndez, N., Soria, A.R., and Skilling,
794 I., 2016, Glacial dropstones in the western Tethys during the late Aptian–early
795 Albian cold snap: Palaeoclimate and palaeogeographic implications for the mid-
796 Cretaceous. Palaeogeography, Palaeoclimatology, Palaeoecology, v. 452, p. 11–27,
797 https://doi.org/10.1016/j.palaeo.2016.04.004.
798 Rodríguez-López, J.P., Meléndez, N., de Boer, P.L., and Soria, A.R., 2008, Aeolian sand
799 sea development along the Mid-Cretaceous Western Tethyan Margin (Spain): erg
800 sedimentology and palaeoclimate implications: Sedimentology, v. 55, p. 1253–
801 1292, https://doi.org/10.1111/j.1365-3091.2007.00945.x.
802 Rodríguez-López, J.P., Wu, C.L., Vishnivetskaya, T.A., Murton, J.B., Tang, W.Q., and
803 Ma, C., 2022, Permafrost in the Cretaceous supergreenhouse: Nature
804 Communications, v. 13, 7946, https://doi.org/10.1038/s41467-022-35676-6.
805 Rodríguez-López, Meléndez, N., de Boer, P.L., and Soria, A.R., 2012. Controls on
806 marine-erg margin cycle variability: aeolian-marine interaction in the Mid-
807 Cretaceous Iberian Desert System, Spain: Sedimentology, v. 59, p. 466–501,
808 https://doi.org/10.1111/j.1365-3091.2011.01261.x.
809 Rogov, M., Ershova, V., Vereshchagin, O., Vasileva, K., Mikhailova, K., and Krylov,
810 A., 2021, Database of global glendonite and ikaite records throughout the
811 Phanerozoic. Earth System Science Data, v. 13, p. 343–356,
812 https://doi.org/10.5194/essd-13-343-2021.
813 Rogov, M.A., Ershova, V.B., Shchepetova, E.V., Zakharov, V.A., Pokrovsky, B.G., and
814 Khudoley, A.K., 2017, Earliest Cretaceous (late Berriasian) glendonites from

Northeast Siberia revise the timing of initiation of transient Early Cretaceous cooling in the high latitudes: Cretaceous Research, v. 71, p. 102–112, https://doi.org/10.1016/j.cretres.2016.11.011.

Rubin, D.M., 1987, Cross-bedding, bedforms and palaeocurrents: SEPM Concepts in Sedimentology and Paleontology 1, 187 p.

Saylor, J.E., and Sundell, K.E., 2016, Quantifying comparison of large detrital geochronology data sets: Geosphere, v. 12, p. 203–220, https://doi.org/10.1130/GES01237.1.

Scherer, C.M.S., Lavina, E.L.C., Dias Filho, D.C., Oliveira, F.M., Bongiolo, D.E., and Aguiar, E.S., 2007, Stratigraphy and facies architecture of the fluvial–aeolian–lacustrine Sergi Formation (Upper Jurassic) Recmŏcavo Basin, Brazil: Sedimentary Geology, v. 194, p. 169–193, https://doi.org/10.1016/j.sedgeo.2006.06.002.

Scherer, C.M.S., Reis, A.D., Horn, B.L.D., Bertolini,G., Lavina, E.L.C., Kifumbi, C., and Aguilar, C.G., 2023, The stratigraphic puzzle of the permo-mesozoic southwestern Gondwana: The Paraná Basin record in geotectonic and palaeoclimatic context: Earth-Science Reviews, v. 240, 104397, https://doi.org/10.1016/j.earscirev.2023.104397.

Shen, C.B., Donelick, R.A., O'Sullivan, P.B., Jonckheere, R., Yang, Z., She, Z.B., Miu, X.L., and Ge, X., 2012a, Provenance and hinterland exhumation from LA-ICP-MS zircon U–Pb and fission-track double dating of Cretaceous sediments in the Jianghan Basin, Yangtze block, central China: Sedimentary Geology, v. 281, p.

194–207, https://doi.org/10.1016/j.sedgeo.2012.09.009.

Shen, C.B., Mei, L.F., Peng, L., Chen, Y., Yang, Z., and Hong, G., 2012b, LA-ICPMS U–Pb zircon age constraints on the provenance of Cretaceous sediments in the Yichang area of the Jianghan Basin, central China: Cretaceous Research, v. 34, p. 172–183, https://doi.org/10.1016/j.cretres.2011.10.016.

Simmons, M.D., 2012, Sequence stratigraphy and sea-level change, *in* Gradstein, F.M., Ogg, J.G., Schmitz, M., and Ogg, G., eds., The Geologic Time Scale 2012: Elsevier 1, p. 239–267.

Skelton, P.W., Spicer, R.A., Kelley, S.P., and Gilmour, I., 2003, The Cretaceous World: Cambridge, Cambridge University Press, 360 p.

Smith, D.G., Cross, T.A., Dufficy, J.P., and Clough, S.R., 1989, Anatomy of an avulsion: Sedimentology, v. 36, p. 1–23, https://doi.org/10.1111/j.1365-3091.1989.tb00817.x.

Sun, Z., Yang, Z., Yang, T., Pei, J., and Yu, Q., 2006, New Late Cretaceous and Paleogene paleomagnetic results from south China and their geodynamic implications: Journal of Geophysical Research: Solid Earth, v. 111, p. 1581–1600, https://doi.org/10.1029/2004JB003455.

Tan, J., Zhang, L.M., Wang, C.S., Cao, K., and Li, X., 2020, Late Cretaceous provenance change in the Jiaolai Basin, East China: Implications for paleogeographic evolution of East Asia: Journal of Asian Earth Sciences, v. 194, 104188, https://doi.org/10.1016/j.jseaes.2019.104188.

Tang, J., Zheng, Y.F., Wu, Y.B., Gong, B., Zha, X.P., and Liu, X.M., 2008, Zircon U–

Pb age and geochemical constraints on the tectonic affinity of the Jiaodong terrane in the Sulu orogen, China: Precambrian Research, v. 161, p. 389–418, https://doi.org/10.1016/j.precamres.2007.09.008.

Todd, S.P., 1989, Stream-driven, high-density gravelly traction carpets: possible deposits in the Trabeg Conglomerate Formation, SW Ireland and some theoretical considerations of their origin: Sedimentology, v. 36, p. 513–530, https://doi.org/10.1111/j.1365-3091.1989.tb02083.x.

Van Itterbeeck, J., Missiaen, P., Folie, A., Markevich, V.S., Van Damme, D., DianYong, G., and Smith, T., 2007, Woodland in a fluvio-lacustrine environment on the dry Mongolian Plateau during the late Paleocene: evidence from the mammal bearing Subeng section (Inner Mongolia, P.R. China): Palaeogeography, Palaeoclimatology, Palaeoecology, v. 243, p. 55–78, https://doi.org/10.1016/j.palaeo.2006.07.005.

Vermeesch, P., 2012, On the visualisation of detrital age distributions: Chemical Geology, 312, 190–194, https://doi.org/10.1016/j.chemgeo.2012.04.021.

Vermeesch, P., 2013, Multi-sample comparison of detrital age distributions: Chemical Geology, v. 341, p. 140–146, https://doi.org/10.1016/j.chemgeo.2013.01.010.

Vermeesch, P., 2018, IsoplotR: A free and open toolbox for geochronology: Geoscience Frontiers, v. 9, p. 1479–1493, https://doi.org/10.1016/j.gsf.2018.04.001.

Vermeesch, P., Resentini, A., and Garzanti, E., 2016, An R package for statistical provenance analysis: Sedimentary Geology, v. 336, p. 14–25, https://doi.org/10.1016/j.sedgeo.2016.01.009.

881 Vickers, M.L., Price, G.D., Jerrett, R.M., Sutton, P., Watkinson, M.P., and Fitzpatrick,
882 M., 2019, The duration and magnitude of Cretaceous cool events: evidence from
883 the northern high latitudes: GSA Bulletin, v. 131, p. 1979–1994,
884 https://doi.org/10.1130/B35074.1.
885 Wan, Y., Liu, D., Xu, M., Zhuang, J., Song, B., Shi, Y., and Du, L., 2007, SHRIMP U–
886 Pb zircon geochronology and geochemistry of metavolcanic and metasedimentary
887 rocks in Northwestern Fujian, Cathaysia block, China: tectonic implications and
888 the need to redefine lithostratigraphic units: Gondwana Research, v. 12, p. 166–
889 183, https://doi.org/10.1016/j.gr.2006.10.016.
890 Wang, D.P., Liu, L., and Frakes, L.A., 1996, The palaeoclimatic and palaeogeographic
891 significance of the Cretaceous red-bed ice-rafting deposits in the Songliao Basin,
892 northeastern China: Sedimentary Facies and Palaeogeography, v. 16, p. 6–11,
893 https://doi.org/CNKI:SUN:YXGD.0.1996-04-001.
894 Wang, D.P., Liu, L., and Frakes, L.A., 1996, The palaeoclimatic and palaeogeographic
895 significance of the Cretaceous red-bed ice-rafting deposits in the Songliao Basin,
896 northeastern China: Sedimentary Facies and Palaeogeography, v. 16, p. 6–11,
897 https://doi.org/CNKI:SUN:YXGD.0.1996-04-001.
898 Wang, J., Chang, S.L., Wang, K.L., Lu, H.B., and Zhang, H.C., 2015a, Geochronology
899 and geochemistry of Early Cretaceous igneous units from the central Sulu
900 orogenic belt: Evidence for crustal delamination during a shift in the regional
901 tectonic regime: Journal of Asian Earth Sciences, v. 112, 49–59.
902 https://doi.org/10.1016/j.jseaes.2015.09.009.

903 Wang, J., Shu, L., Santosh, M., and Xu, Z., 2015b, The Pre-Mesozoic crustal evolution
904 of the Cathaysia Block, South China: Insights from geological investigation,
905 zircon U–Pb geochronology, Hf isotope and REE geochemistry from the
906 Wugongshan complex: Gondwana Research, v. 28, p. 225–245,
907 https://doi.org/10.1016/j.gr.2014.03.008.
908 Wang, L., Yu, J., O'Reilly, S., Griffin, W., Sun, T., Wei, Z., Jiang, S., and Shu, L., 2008,
909 Grenvillian orogeny in the Southern Cathaysia Block: Constraints from U-Pb ages
910 and Lu-Hf isotopes in zircon from metamorphic basement: Chinese Science
911 Bulletin, v. 53, p. 3037–3050, https://doi.org/10.1007/s11434-008-0262-0.
912 Wang, L.J., Griffin, W.L., Yu, J.H., and O'Reilly, S.Y., 2010a, Precambrian crustal
913 evolution of the Yangtze Block tracked by detrital zircons from Neoproterozoic
914 sedimentary rocks: Precambrian Research, v. 177, p. 131–144,
915 https://doi.org/10.1016/j.precamres.2009.11.008.
916 Wang, L.J., Griffin, W.L., Yu, J.H., and O'Reilly, S.Y., 2013a, U–Pb and Lu–Hf isotopes
917 in detrital zircon from Neoproterozoic sedimentary rocks in the northern Yangtze
918 Block: Implications for Precambrian crustal evolution: Gondwana Research, v. 23,
919 p. 1261–1272, https://doi.org/10.1016/j.gr.2012.04.013.
920 Wang, L.J., Yu, J.H., Griffin, W.L., and O'Reilly, S.Y., 2012a, Early crustal evolution
921 in the western Yangtze Block: Evidence from U–Pb and Lu–Hf isotopes on detrital
922 zircons from sedimentary rocks: Precambrian Research, v. 222–223, p. 368–385,
923 https://doi.org/10.1016/j.precamres.2011.08.001.
924 Wang, W., Wang, F., Chen, F., Zhu, X., Xiao, P., and Siebel, W., 2010b, Detrital zircon

925 ages and Hf-Nd isotopic composition of neoproterozoic sedimentary rocks in the
926 Yangtze Block: constraints on the deposition age and provenance: The Journal of
927 Geology, v. 118, p. 79–94, https://doi.org/10.1086/648533.
928 Wang, W., Zhou, M.F., Yan, D.P., Li, L., and Malpas, J., 2013b, Detrital zircon record
929 of Neoproterozoic active-margin sedimentation in the eastern Jiangnan Orogen,
930 South China: Precambrian Research, v. 235, p. 1–19,
931 https://doi.org/10.1016/j.precamres.2013.05.013.
932 Wang, X.C., Li, X.h., Li, Z.X., Li, Q.l., Tang, G.Q., Gao, Y.Y., Zhang, Q.R., and Liu,
933 Y., 2012b, Episodic Precambrian crust growth: evidence from U–Pb ages and Hf–
934 O isotopes of zircon in the Nanhua Basin, central South China: Precambrian
935 Research, v. 222, p. 386–403, https://doi.org/10.1016/j.precamres.2011.06.001.
936 Wang, Y., Xiang, B., Zhu, G., and Jiang, D., 2011, Structural and geochronological
937 evidence for Early Cretaceous orogen-parallel extension of the ductile lithosphere
938 in the northern Dabie orogenic belt, East China: Journal of Structural Geology, v.
939 33, p. 362–380, https://doi.org/10.1016/j.jsg.2010.09.002.
940 Wang, Y., Zhang, F., Fan, W., Zhang, G., Chen, S., Cawood, P.A., and Zhang, A., 2010c,
941 Tectonic setting of the South China Block in the early Paleozoic: Resolving
942 intracontinental and ocean closure models from detrital zircon U-Pb
943 geochronology: Tectonics, v. 29, TC6020, https://doi.org/10.1029/2010TC002750.
944 Wang, Y.C., Peng, N., Kuang, H.W., Zhao, F.H., Liu, Y.Q., Yang, Z.R., Cui, M.G., Chen,
945 X.S., Qiao, D.W., and Qi, K.N., 2023, Relict sand wedges suggest a high altitude
946 and cold temperature during the Early Cretaceous in the Ordos Basin, North China:

947 International Geology Review, v. 65, p. 900–919,
948 https://doi.org/10.1080/00206814.2022. 2081938.
949 Wu, C.H., and Rodríguez-López, J.P., 2021, Cryospheric processes in Quaternary and
950 Cretaceous hyper-arid plateau desert oases: Sedimentology, v. 68, p. 755–770,
951 https://doi.org/10.1111/sed.12804.
952 Wu, C.H., Rodríguez-López, J.P., and Santosh, M., 2022, Plateau archives of
953 lithosphere dynamics, cryosphere and paleoclimate: The formation of Cretaceous
954 desert basins in East Asia: Geoscience Frontiers, v. 13, 101454,
955 https://doi.org/10.1016/j.gsf.2022.101454.
956 Wu, L., Jia, D., Li, H., Deng, F., and Li, Y., 2010, Provenance of detrital zircons from
957 the late Neoproterozoic to Ordovician sandstones of South China: Implications for
958 its continental affinity: Geological Magazine, v. 147, p. 974–980,
959 https://doi:10.1017/S0016756810000725.
960 Xia, G.Q., Wu, C.L., Mansour, A., Jin, X., and Yi, H.S., 2023, Eocene–Oligocene
961 glaciation on a high central Tibetan Plateau: Geology, v. 51, p. 559–564,
962 https://doi.org/10.1130/G51104.1.
963 Xiang, L., and Shu, L., 2010, Pre-Devonian tectonic evolution of the eastern South
964 China Block: Geochronological evidence from detrital zircons: Science China
965 Earth Sciences, v. 53, p. 1427–1444, https://doi.org/10.1007/s11430-010-4061-5.
966 Xie, C.L., Chen, J., Liu, Y.Q., Zhu, X.C., Niu, M.L., and Xiang, B.W., 2016, Inherited
967 zircon U-Pb geochronology of the Late Mesozoic igneous rocks from the
968 Zhangbaling uplift segment of the Tan-Lu Fault Zone: Magma source affinity and

its tectonic implications: Acta Petrologica Sinica, v. 32, p. 976–1000.

Xie, S.W., Wu, Y.B., Zhang, Z.M., Qin, Y.C., Liu, X.C., Wang, H., Qin, Z.W., Liu, Q., and Yang, S.H., 2012, U-Pb ages and trace elements of detrital zircons from Early Cretaceous sedimentary rocks in the Jiaolai Basin, north margin of the Sulu UHP terrane: Provenances and tectonic implications: Lithos, v. 154, p. 346–360, https://doi.org/10.1016/j.lithos.2012.08.002.

Xu, H.J., Zhang, J.F., Wang, Y.F., and Liu, W.L., 2016, Late Triassic alkaline complex in the Sulu UHP terrane: implications for post-collisional magmatism and subsequent fractional crystallization: Gondwana Research, v. 35, p. 390–410, https://doi.org/10.1016/j.gr.2015.05.017.

Xu, Y., Du, Y., Cawood, P.A., Zhu, Y., Li, W., and Yu, W., 2012, Detrital zircon provenance of Upper Ordovician and Silurian strata in the northeastern Yangtze Block: Response to orogenesis in South China: Sedimentary Geology, v. 267, p. 63–72, https://doi.org/10.1016/j.sedgeo.2012.05.009.

Yan, Y., Hu, X.Q., Lin, G., Santosh, M., and Chan, L.S., 2011, Sedimentary provenance of the Hengyang and Mayang basins, SE China, and implications for the Mesozoic topographic change in South China Craton: Evidence from detrital zircon geochronology: Journal of Asian Earth Sciences, v. 41, p. 494–503, https://doi.org/10.1016/j.jseaes.2011.03.012.

Yan, Z., Wang, Z.Q., Chen, J.L., Yan, Q.R., and Wang, T., 2010, Detrital record of Neoproterozoic arc-magmatism along the NW margin of the Yangtze Block, China: U–Pb geochronology and petrography of sandstones: Journal of Asian Earth

991 Sciences, v. 37, p. 322–334, https://doi.org/10.1016/j.jseaes.2009.09.001.
992 Yang, C., Li, X.H., Wang, X.C., and Lan, Z., 2015a, Mid-Neoproterozoic angular
993 unconformity in the Yangtze Block revisited: Insights from detrital zircon U–Pb
994 age and Hf–O isotopes: Precambrian Research, v. 266, p. 165−178,
995 https://doi.org/10.1016/j.precamres.2015.05.016.
996 Yang, D.B., Xu, W.L., Xu, Y.G., Wang, Q.H., Pei, F.P., and Wang, F., 2012, U–Pb ages
997 and Hf isotope data from detrital zircons in the Neoproterozoic sandstones of
998 northern Jiangsu and southern Liaoning Provinces, China: Implications for the
999 Late Precambrian evolution of the southeastern North China Craton: Precambrian
1000 Research, v. 216, p. 162–176, https://doi.org/10.1016/j.precamres.2012.07.002.
1001 Yang, J.H., Chung, S.L., Wilde, S.A., Wu, F.Y., Chu, M.F., Lo, C.H., and Fan, H.R.,
1002 2005, Petrogenesis of post-orogenic syenites in the Sulu Orogenic Belt, East China:
1003 geochronological, geochemical and Nd–Sr isotopic evidence: Chemical Geology,
1004 v. 214, p. 99–125, https://doi.org/10.1016/j.chemgeo.2004.08.053.
1005 Yang, J.S., Li, T.F., Chen, S.Z., Wu, C.L., Robinson, P.T., Liu, D.Y., and Wooden, J.L.,
1006 2009, Genesis of garnet peridotites in the Sulu UHP belt: examples from the
1007 Chinese continental scientific drilling project-main hole, PP1 and PP3 drillholes:
1008 Tectonophysics, v. 475, p. 359–382, https://doi.org/10.1016/j.tecto.2009.02.032.
1009 Yang, J.S., Wooden, J.L., Wu, C.L., Liu, F.L., Xu, Z.Q., Shi, R.D., Katayama, I., Liou,
1010 J.G., and Maruyama, S., 2003, SHRIMP U-Pb dating of coesite-bearing zircon
1011 from the ultrahigh-pressure metamorphic rocks, Sulu terrane, east China: Journal
1012 of Metamorphic Geology, v. 21, p. 551–560, https://doi.org/10.1046/j.1525-

1314.2003.00463.x.

Yang, W.B., Niu, H.C., Sun, W.D., Shan, Q., Zheng, Y.F., Li, N.B., Li, C.Y., Arndt, N.T., Xu, X., Jiang, Y.H., and Yu, X.Y., 2013, Isotopic evidence for continental ice sheet in mid-latitude region in the supergreenhouse Early Cretaceous: Scientific Reports, v. 3, 2732, https://doi.org/10.1038/srep02732.

Yang, Y.T., 2013, An unrecognized major collision of the Okhotomorsk block with East Asia during the late cretaceous, constraints on the plate reorganization of the northwest pacific: Earth-Science Reviews, v. 126, p. 96–115, https://doi.org/10.1016/j.earscirev.2013.07.010.

Yang, Z., Yang, K., Xu, Y., Deng, X., Cheng, W., and Long, Z., 2015b, Zircon U-Pb geochronology, Hf isotopic composition, and geological implications of the Neoproterozoic meta-sedimentary rocks in Suizhou-Zaoyang area, the northern Yangtze Block: Science China Earth Sciences, v. 58, p. 1910–1923, https://doi.org/10.1007/s11430-015-5073-y.

Yao, J., Shu, L., and Santosh, M., 2011, Detrital zircon U–Pb geochronology, Hf-isotopes and geochemistry—new clues for the Precambrian crustal evolution of Cathaysia Block, South China: Gondwana Research, v. 20, p. 553–567, https://doi.org/10.1016/j.gr.2011.01.005.

Yao, J., Shu, L., Santosh, M., and Xu, Z., 2014a, Palaeozoic metamorphism of the Neoproterozoic basement in NE Cathaysia: zircon U–Pb ages, Hf isotope and whole-rock geochemistry from the Chencai Group: Journal of the Geological Society, v. 171, p. 281–297, https://doi.org/10.1144/jgs2013-0.

1035 Yao, W.H., Li, Z.X., Li, W.X., Li, X.H., and Yang, J.H., 2014b, From Rodinia to
1036 Gondwanaland: A tale of detrital zircon provenance analyses from the southern
1037 Nanhua Basin, South China: American Journal of Science, v. 314, p. 278–313,
1038 https://doi.org/10.2475/01.2014.08.
1039 Yu, J.H., O'Reilly, S.Y., Wang, L., Griffin, W., Zhang, M., Wang, R., Jiang, S., and Shu,
1040 L., 2008, Where was South China in the Rodinia supercontinent?: evidence from
1041 U–Pb geochronology and Hf isotopes of detrital zircons: Precambrian Research,
1042 v. 164, p. 1–15, https://doi.org/10.1016/j.precamres.2008.03.002.
1043 Yu, J.H., O'Reilly, S.Y., Wang, L., Griffin, W.L., Zhou, M.F., Zhang, M., and Shu, L.,
1044 2010, Components and episodic growth of Precambrian crust in the Cathaysia
1045 Block, South China: evidence from U–Pb ages and Hf isotopes of zircons in
1046 Neoproterozoic sediments: Precambrian Research, v. 181, p. 97–114,
1047 https://doi.org/10.1016/j.precamres.2010.05.016.
1048 Yu, W., Du, Y., Cawood, P.A., Xu, Y., and Yang, J., 2015, Detrital zircon evidence for
1049 the reactivation of an Early Paleozoic syn-orogenic basin along the North
1050 Gondwana margin in South China: Gondwana Research, v. 28, p. 769–780,
1051 https://doi.org/10.1016/j.gr.2014.07.014.
1052 Yu, X.C., Liu, C.L., Wang, C.L., and Wang, J.Y., 2021. Late Cretaceous aeolian desert
1053 system within the Mesozoic fold belt of South China: palaeoclimatic changes and
1054 tectonic forcing of East Asian erg development and preservation:
1055 Palaeogeography, Palaeoclimatology, Palaeoecology, v. 567, 110299,
1056 https://doi.org/10.1016/j.palaeo.2021.110299.

Yue, W.Z., and Ding, B.L., 1999, Study on Cretaceous stratigraphic sequence of continental basin in Jiangsu: Volcanology & Mineral Resources, v. 20, p. 287–344, https://doi.org/CNKI:SUN:HSDZ.0.1999-04-001.

Yue, W.Z., Ye, Z.Z., and Jiang, Y.H., 1997, Sedimentary environment of the Late Cretaceous Chishan Formation in Jiangsu Province: Acta Sedimentologica Sinica, v. 15, p. 1–7, https://doi.org/10.14027/j.cnki.cjxb.1997.s1.013.

Zhang, J., Liu, Y.G., Flögel, S., Zhang, T., Wang, C.S., and Fang, X.M., 2021, Altitude of the East Asian coastal mountains and their influence on Asian climate during early Late Cretaceous: Journal of Geophysical Research: Atmospheres, v. 126, e2020JD034413, https://doi. org/10.1029/2020JD034413.

Zhang, J., Zhao, Z.F., Zheng, Y.F., and Dai, M.N., 2010, Postcollisional magmatism: geochemical constraints on the petrogenesis of Mesozoic granitoids in the Sulu orogen, China: Lithos, v. 119, p. 512–536, https://doi.org/10.1016/j.lithos.2010.08.005.

Zhang, J., Zhao, Z.F., Zheng, Y.F., Liu, X.M., and Xie, L.W., 2012, Zircon Hf–O isotope and whole-rock geochemical constraints on origin of postcollisional mafic to felsic dykes in the Sulu orogen: Lithos, v. 136–139, p. 225–245, https://doi.org/10.1016/j.lithos.2011.06.006.

Zhang, L.M., Wang, C.S., Cao, K., Wang, Q., Tan, J., and Gao, Y., 2016, High elevation of Jiaolai basin during the late cretaceous: Implication for the coastal mountains along the East Asian margin: Earth and Planetary Science Letters, v. 456, p. 112–123, https://doi.org/10.1016/j.epsl.2016.09.034.

1079 Zhang, R.Y., Yang, J.S., Wooden, J.L., Liou, J.G., and Li, T.F., 2005, U–Pb SHRIMP
1080 geochronology of zircon in garnet peridotite from the Sulu UHP terrane, China:
1081 Implications for mantle metasomatism and subduction-zone UHP metamorphism:
1082 Earth and Planetary Science Letters, v. 237, p. 729–743,
1083 https://doi.org/10.1016/j.epsl.2005.07.003.
1084 Zhang, S.B., Zheng, Y.F., Wu, Y.B., Zhao, Z.F., Gao, S., and Wu, F.Y., 2006b, Zircon
1085 U–Pb age and Hf isotope evidence for 3.8 Ga crustal remnant and episodic
1086 reworking of Archean crust in South China: Earth and Planetary Science Letters,
1087 v. 252, p. 56–71, https://doi.org/10.1016/j.epsl.2006.09.027.
1088 Zhang, S.B., Zheng, Y.F., Wu, Y.B., Zhao, Z.F., Gao, S., and Wu, F.Y., 2006a, Zircon
1089 isotope evidence for ≥3.5 Ga continental crust in the Yangtze craton of China:
1090 Precambrian Research, v. 146, p. 16–34,
1091 https://doi.org/10.1016/j.precamres.2006.01.002.
1092 Zhao, R., Wang, Q.F., Liu, X.F., Wang, W., and Pan, R.G., 2016, Architecture of the
1093 Sulu crustal suture between the North China Craton and Yangtze Craton:
1094 Constraints from Mesozoic granitoids: Lithos, v. 266–267, p. 348–361,
1095 https://doi.org/10.1016/j.lithos.2016.10.018.
1096 Zhao, T., Zhu, G., Lin, S.Z., Yan, L.J., and Jiang, Q.Q., 2014, Protolith ages and
1097 deformation mechanism of metamorphic rocks in the Zhangbaling Uplift segment
1098 of the Tan–Lu Fault Zone: Science China Earth Sciences, v. 57, p. 2740–2757,
1099 https://doi.org/10.1007/s11430-014-4959-4.
1100 Zhou, J.B., Simon, A.W., Liu, F.L., and Han, J., 2012, Zircon U–Pb and Lu–Hf isotope

study of the Neoproterozoic Haizhou Group in the Sulu Orogen: provenance and tectonic implications: Lithos, v. 136–139, p. 261–281, https://doi.org/10.1016/j.lithos.2011.01.015.

Figure captions

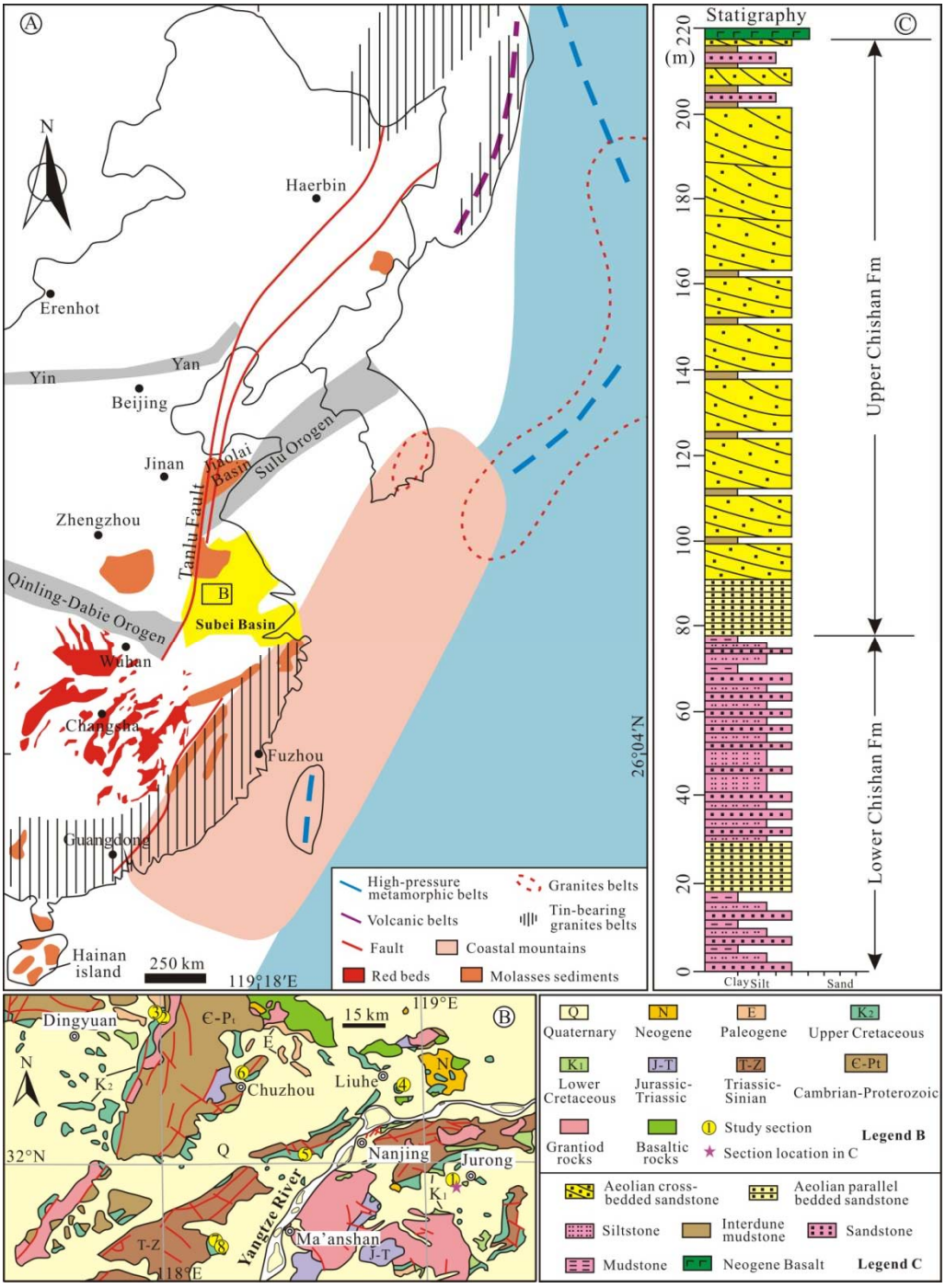

Figure 1. Geological map and stratigraphic section at the East Asian continental margin during the Late Cretaceous. (A) Key geological features and location of the Subei Basin (modified from Zhang et al., 2016). The range of the coastal mountains is based on the interpretations of Chen (1997) and Yang (2013). (B) Geologic map of the study area in the Subei Basin. (C) Stratigraphy of the Chishan Formation of the Subei Basin. The stratigraphic section is modified from Yue et al. (1997).

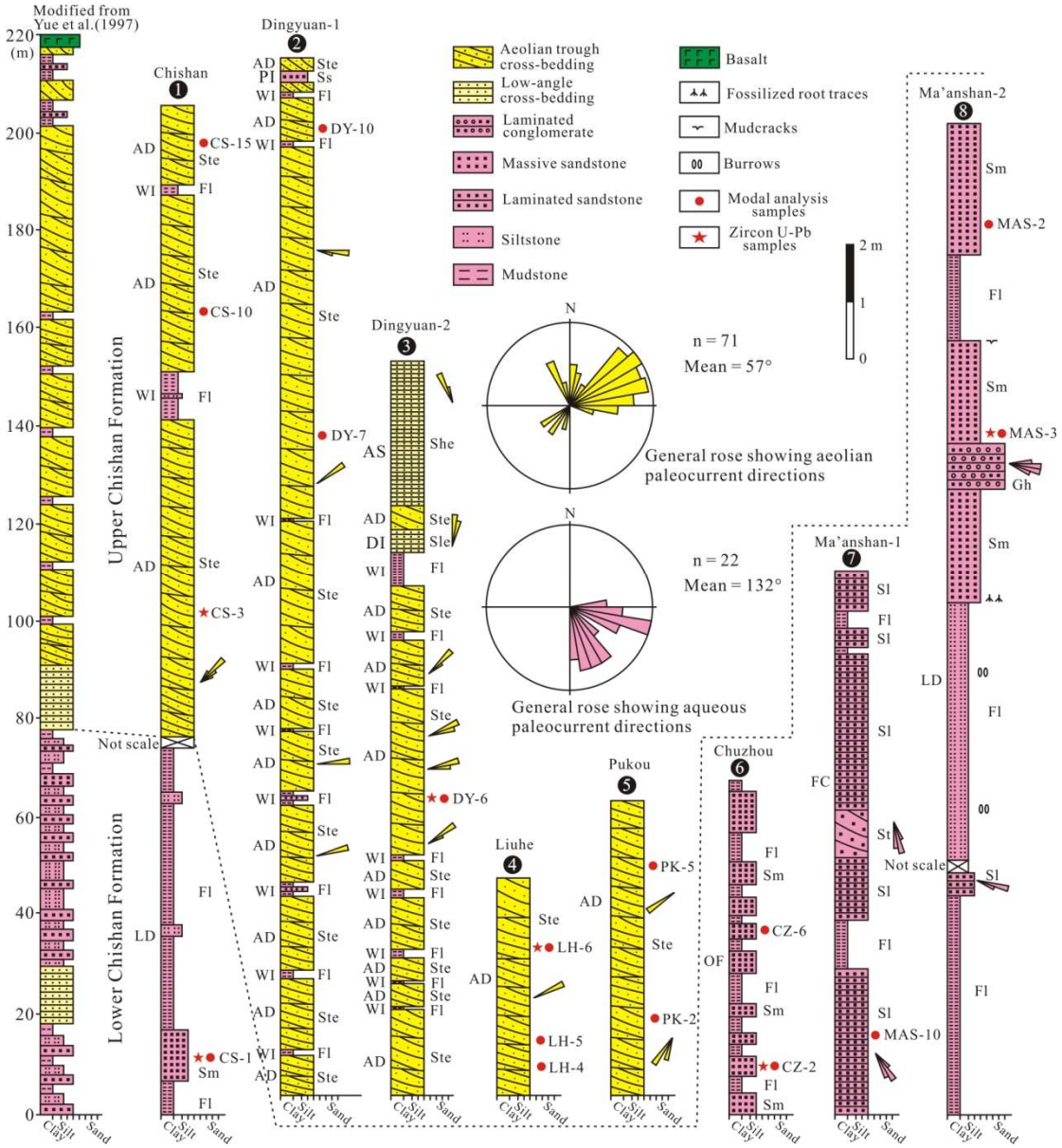

Figure 2. Sedimentary logs of the studied outcrop sections of the Chishan

Formation. Paleocurrents are presented. The location of these sections is shown in Figure 1A. See Table 1 for facies codes and facie associations.

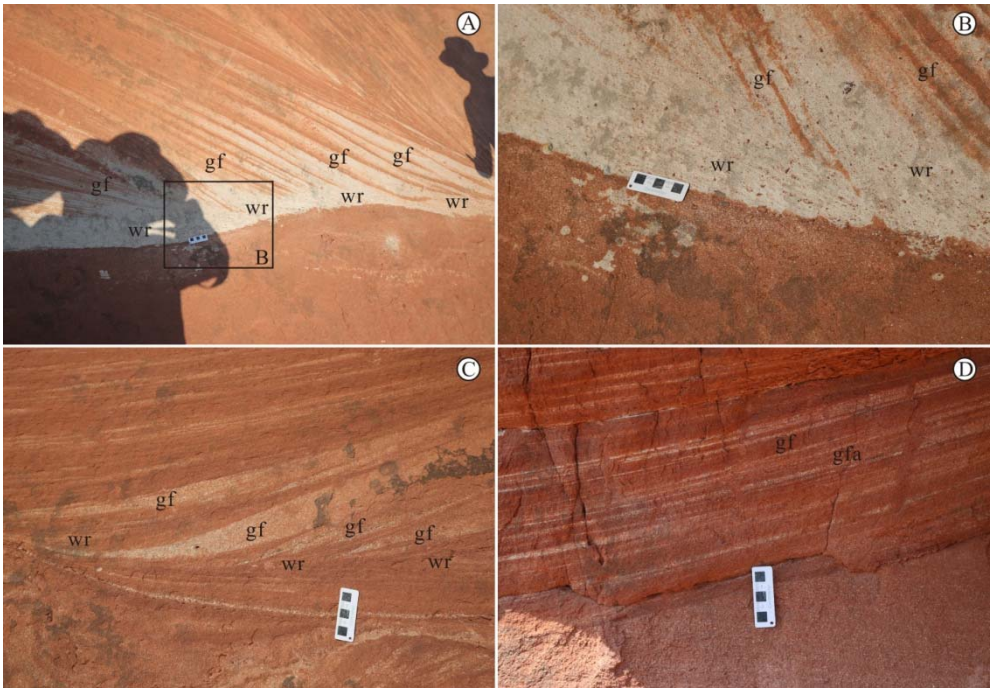

Figure 3. Internal stratification in the trough cross-bedded sets. (A−C) Alternating wind-ripple laminae (wr) and grainflow strata (gf). (D) Interbedding of grainflow (gf) and grainfall (gfa) deposits in the trough cross-bedded sets.

Figure 4. Dune–wet interdune intertonguing and associated mud intraclasts and

dropstones in the Upper Chishan Formation of the Subei Basin. (A) Interdune mudstone intraclasts due to the compaction of the overlying aeolian dune toeset sandstones. Geologist for scale is 1.8 m tall. (B) Aeolian dune toesets pinch-out into strata of wet interdune origin where a sandy conglomerate cobble occurs. Hammer for scale is 38 cm long. See table 1 for facies codes.

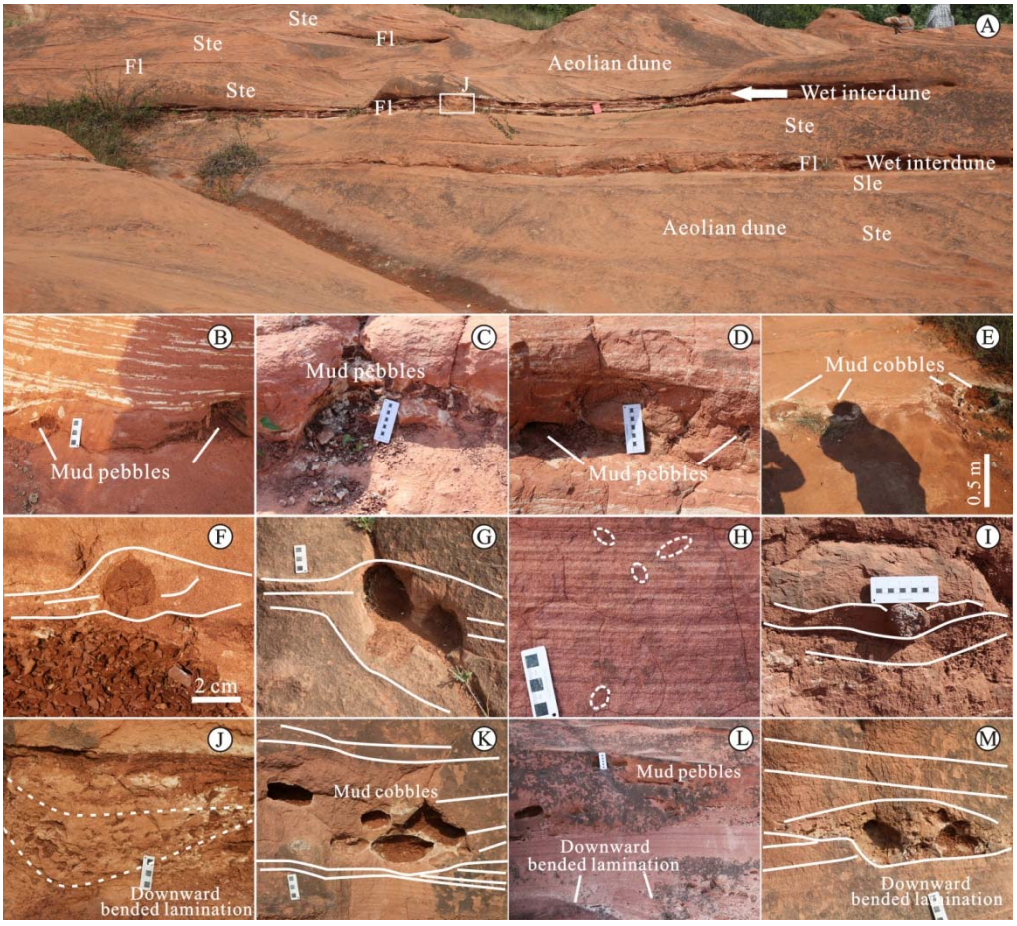

Figure 5. Dune–wet interdune intertonguing and associated mud intraclasts, dropstones and massive diamicton deposits in the Upper Chishan Formation of the Subei Basin. (A) Massive diamicton occurs in wet interdune. The field notebook is 18.2 long and 12.5 wide. See table 1 for facies codes. (B−E) Mud intraclasts in the interdune facies. (F−H) The underlying laminations are bent and disrupted as a result of the dropstones hitting the interdune laminations. (I) A

dropstone of sandy conglomerate cobble. The underlying laminations are deformed and disrupted, whilst the top of the dropstone is draped by the overlying laminations. (J) Close-up view from (A) showing downward bended lamination. (K) Mud cobbles with its longest axis perpendicular, inclined or parallel to lamination. (L) and (M) Lenticular diamicton deposits develop in the laminated sandstones, which themselves show down-bent lamination at the bottom and draped lamination at the top.

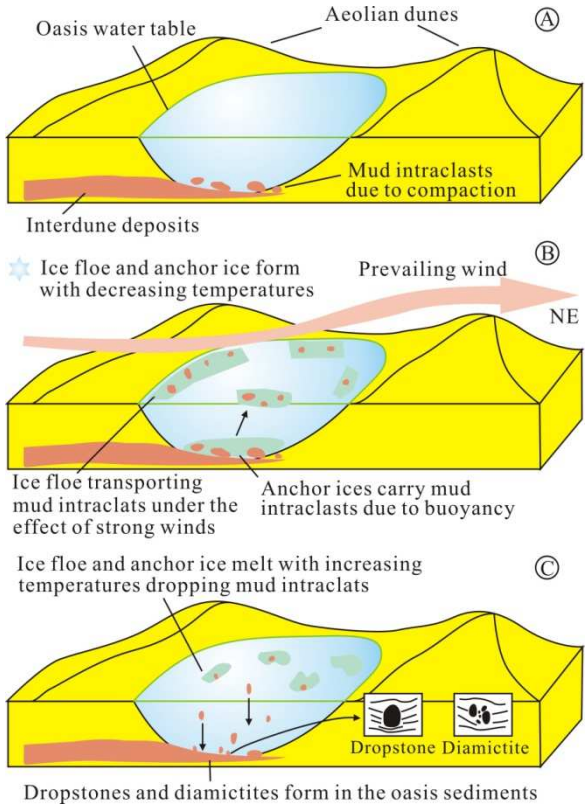

Figure 6. Schematic model interpreting cryospheric processes on plateau desert oases (modified from Wu and Rodríguez-López, 2021). (A) Differential compaction between aeolian dune sandstones and wet interdune deposits generates mud intraclasts, which occur at the same stratigraphic level as adjacent undeformed parent interdune deposits. (B) Anchor ice forms in the oasis bottom

and ice floe forms in the oasis water surface with plateau desert temperatures reaching −12 ℃. Strong westerlies blowing over the oasis water lead to cracking of ice floes, which transport mudclasts derived from erosion of the margins of the oases. At the same time, anchor ices carry mudclasts to the oasis water surface. (C) Ice floe and anchor ice melt with increasing plateau desert temperatures, which drop mud intraclasts and lead to the development of dropstones and diamictites in the oasis bottom sediments.

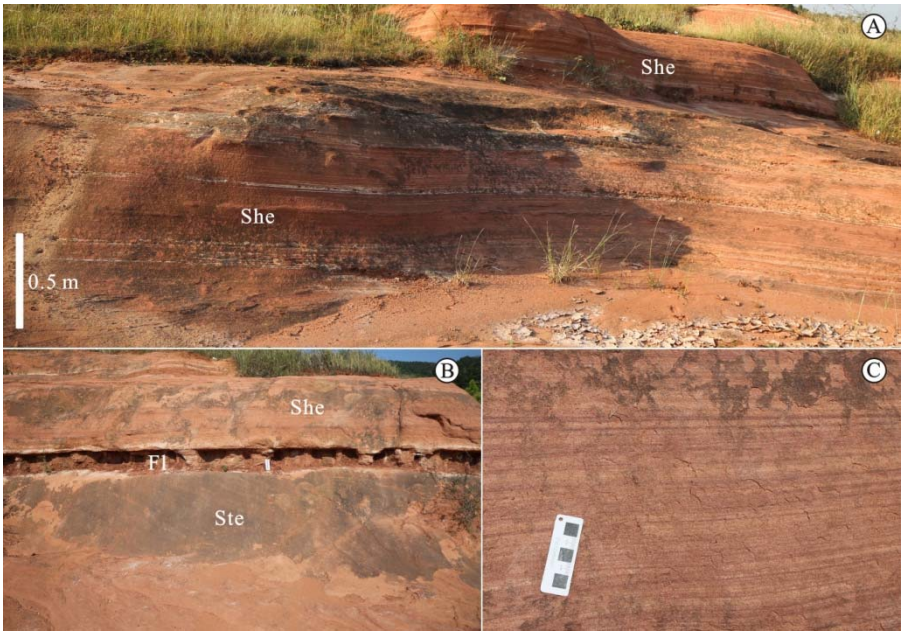

Figure 7. Aeolian sandsheet deposits in the Upper Chishan Formation. (A) isolated horizontal to subhorizontal laminated sandstones (She). (B) Laminated sandstones (She) overlie thin-beded musdtones (Fl). (C) Subcritically climbing translatent strata showing inversely grading.

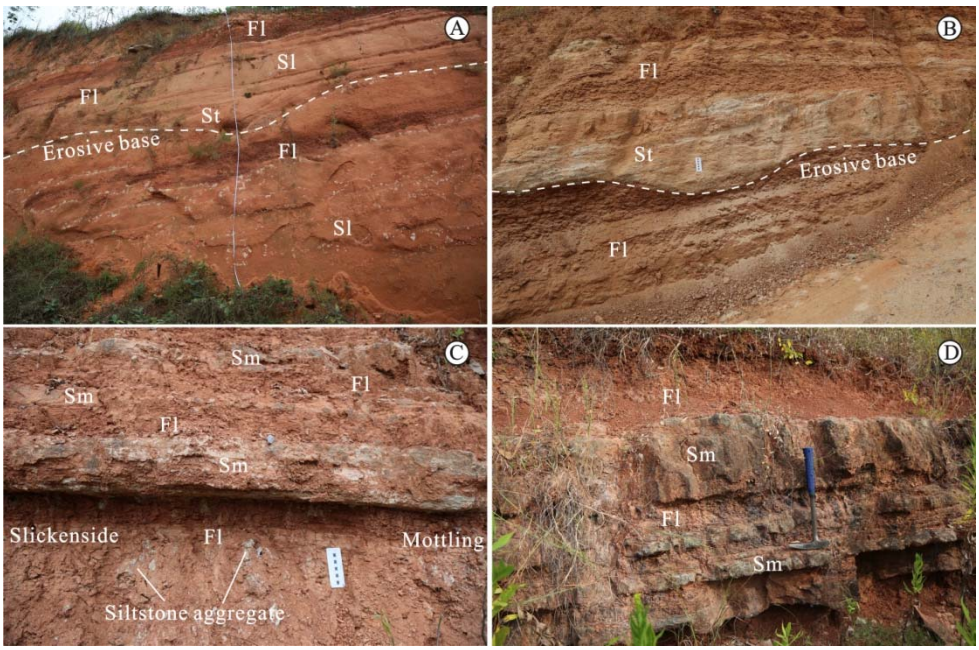

1161

1162 **Figure 8. Fluvial channel and overbank flood deposits in the Lower Chishan**
1163 **Formation. (A) Vertical stacking of trough cross-bedded sandstones (St), low-angle**
1164 **cross-bedded sandstones (Sl) and thinly bedded or lenticular purple mudstones**
1165 **(Fl). (B) Trough cross-bedded sandstones (St) bounded by erosive bases overlie the**
1166 **mudstone layer. (C) Alternating tabular sandstones (Sm) and laminated silty**
1167 **mudstones (Fl). Thick silty mudstones represent pale grey-green mottling, siltstone**
1168 **aggregates and slickensides. (D) Interbedded massive tabular sandstones (Sm) and**
1169 **mudstones (Fl). Hammer for scale is 38 cm long.**

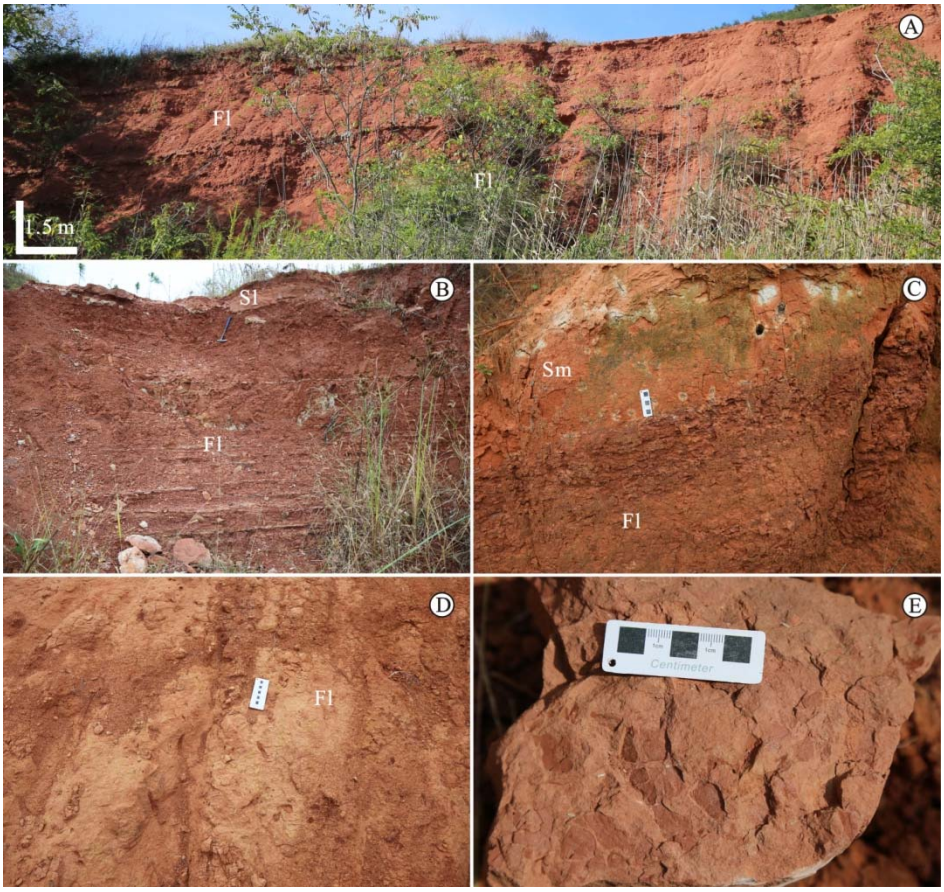

1170

1171 **Figure 9. Lake deposits in the Lower Chishan Formation. (A) Alternating thick-**

1172 **bedded silty mudstones and thin-bedded siltstones (Fl). (B) Thin-bedded low-angle**

1173 **cross-bedded sandstones overlie thick-bedded silty mudstones (Fl). Hammer for**

1174 **scale is 38 cm long. (C) Thick mudstones (Fl) overlain by massive sandstones (Sm).**

1175 **Fossilized root traces occur at the base of massive sandstones. (D) Burrows are**

1176 **developed in the silty sediments. (E) Mudcracks occur atop the muddy sandstones.**

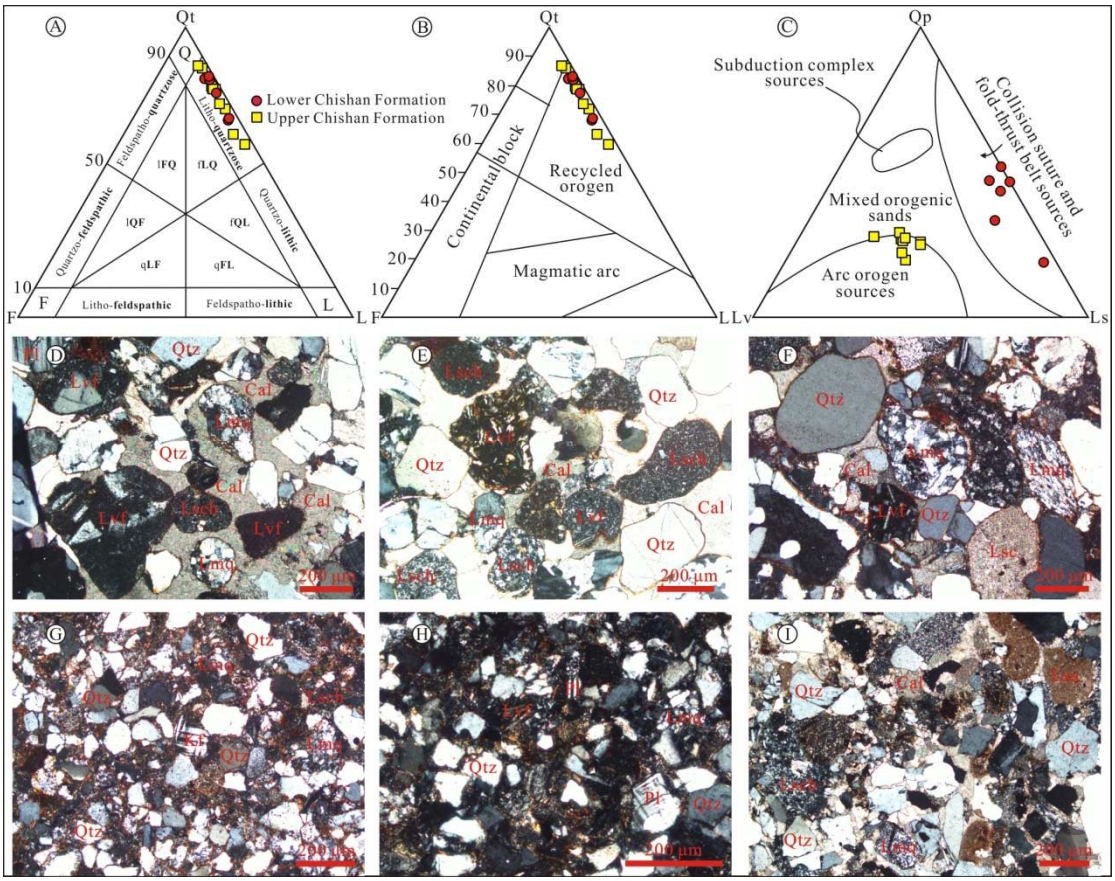

Figure 10. Petrography and modal grain compositions of sandstones from the Chishan Formation. (A) Petrographic classification for sandstones (Garzanti (2016). (B) and (C) Provisional compositional fields for different types of provenance (Dickinson, 1985; Garzanti, 2016). (D−F) Petrography of sandstones from the Upper Chishan Formation. (G−I) Petrography of sandstones from the Lower Chishan Formation. Qtz, quartz; Qp, polycrystalline quartz; Qt, total quartz; F, total feldspar; Kf, K-feldspar; Pl, plagioclase; L, total lithics; Ls, sedimentary lithic fragments; Lss, sedimentary siltstone fragments; Lsch, sedimentary chert fragments; Lsc, sedimentary carbonate fragments; Lv, volcanic lithic fragments; Lvf, volcanic felsic fragments; Lmp, metamorphic quartzite fragments; Cal, calcite.

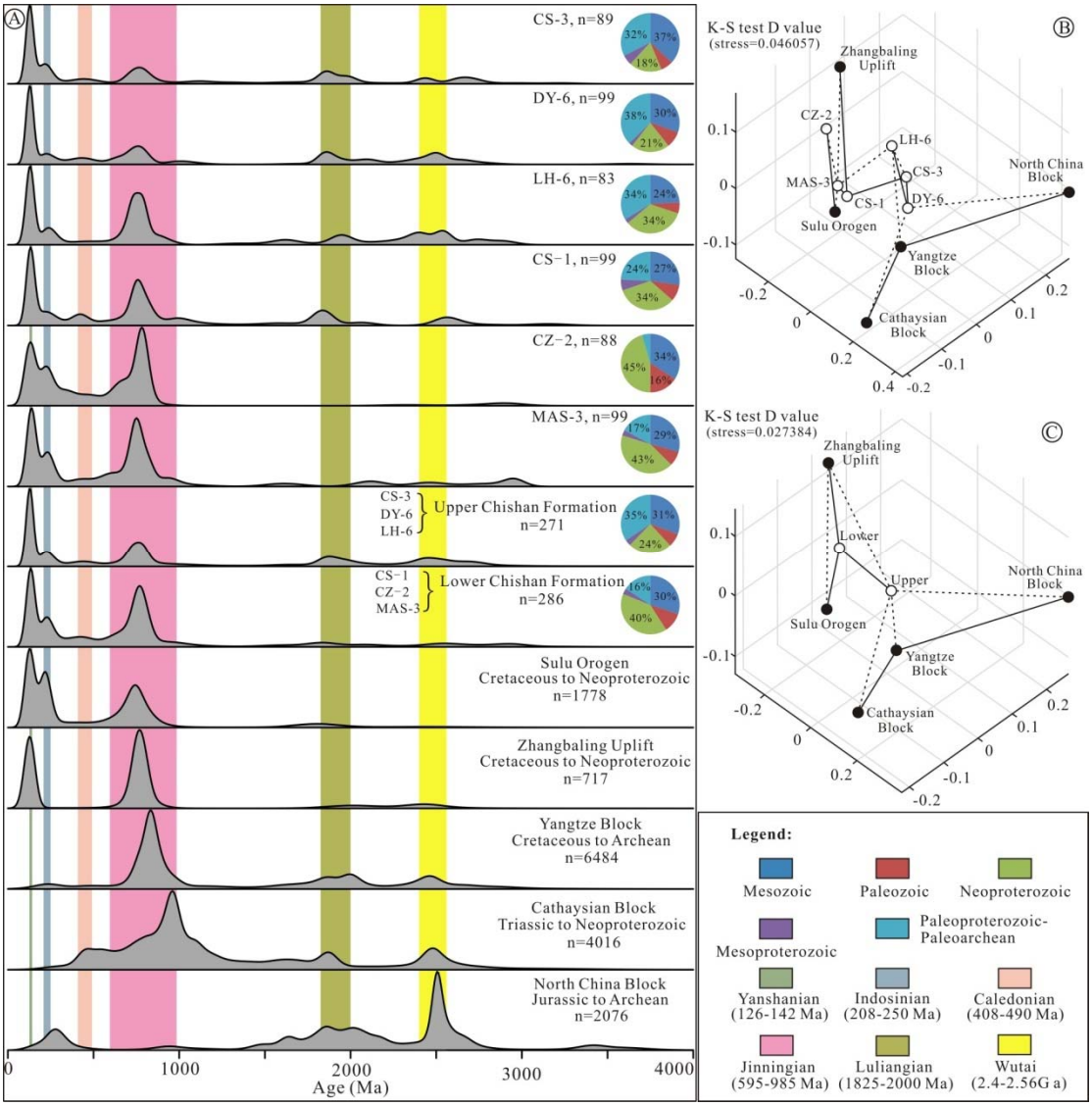

Figure 11. Kernel Density Estimate plots (KDE) and three dimensional multidimensional scaling (MDS) for all samples and source terranes. (A) Comparison of KDE of detrital zircon U-Pb ages from the Chishan Formation with potential source terranes. (B) MDS of detrital zircon U-Pb ages for studied sandstone samples and potential source terranes. (C) MDS for the Lower and Upper Chishan Formation and potential source terranes. K-S test D value is used to determine dissimilarity. Pie diagrams show the ratios of five major periods. Sandstone samples (CS-1, CZ-2 and MAS-3) are from the lower Chishan Formation; and sandstone samples (CS-3, DY-6 and LH-6) are from the upper

Chishan Formation. Six major age peaks are Yanshanian (126−142 Ma), Indosinian (208−250 Ma), Caledonian (408−490 Ma), Jinningian (595−985 Ma), Luliangian (1825−2000 Ma), and Wutai (2400−2560 Ma). Data sources: Sulu Orogen (Yang et al., 2003; Liu et al., 2004; Yang et al., 2005; Zhang et al., 2005; Huang et al., 2006; Liou et al., 2006; Liu et al., 2008a, Tang et al., 2008; Katsube et al., 2009; Yang et al., 2009; Zhang et al., 2010; Charles et al., 2011; Lan et al., 2011; Liu et al., 2011; Wang et al., 2011; Xie et al., 2012; Zhang et al., 2012; Zhou et al., 2012; Chen et al., 2013; Wang et al., 2015a; Li et al., 2016; Xu et al., 2016; Zhao et al., 2016), Zhangbaling Uplift (Niu et al., 2008, 2020; Zhao et al., 2014; Xie et al., 2016; Li et al., 2021), Yangtze Block (Zhang et al., 2006a, b; Liu et al., 2008b; Wang et al., 2010a, b; Yan et al., 2011; Duan et al., 2012; Shen et al., 2012a, b; Wang et al., 2012a, b; Xu et al., 2012; Li et al., 2013a; Wang et al., 2013a, b; Yang et al., 2015a, b; Yu et al., 2015), Cathaysian Block (Wan et al., 2007; Wang et al., 2008; Yu et al., 2008; Wang et al., 2010c; Wu et al., 2010; Xiang et al., 2010; Yu et al., 2010; Li et al., 2011; Yao et al., 2011; Li et al., 2012; Yao et al., 2014a, b; Wang et al., 2015b), and North China Block (Darby et al., 2006; Diwu et al., 2008; Li et al., 2008a, b; Li et al., 2010; Du et al., 2012; Yang et al., 2012; Li et al., 2013b; Liu et al., 2013; Li et al., 2015).

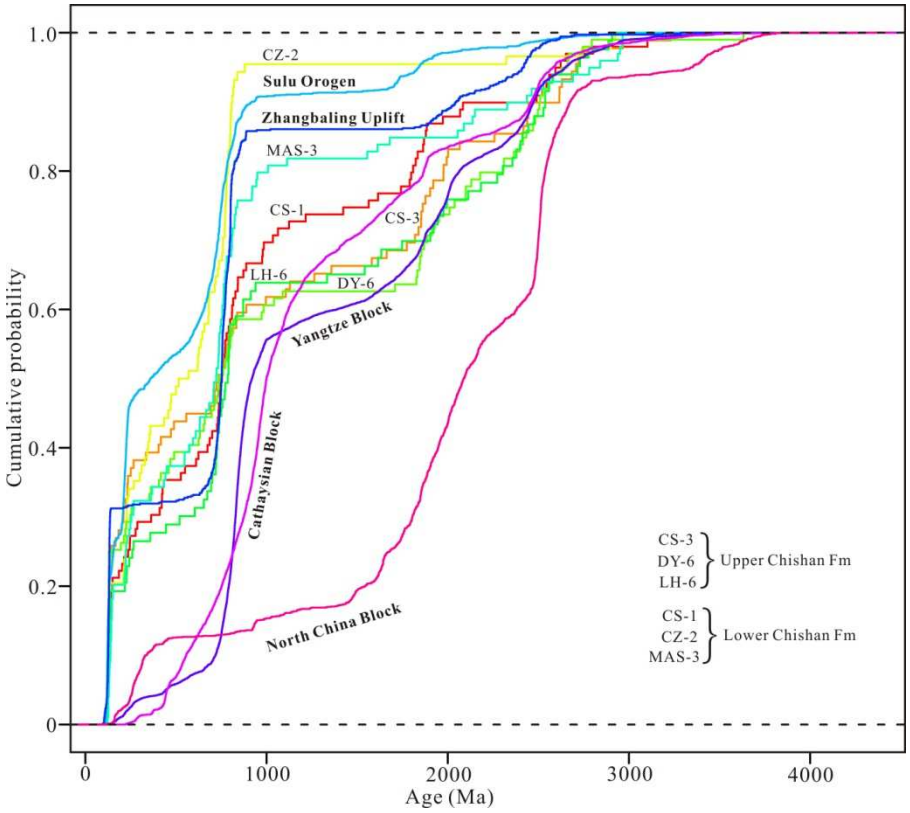

1217

1218 **Figure 12. Cumulative probability densities plots (CPD) for all sandstone samples**

1219 **in comparison to potential major sources. Detrital zircon age data are similar to**

1220 **those used in Figure 5.**

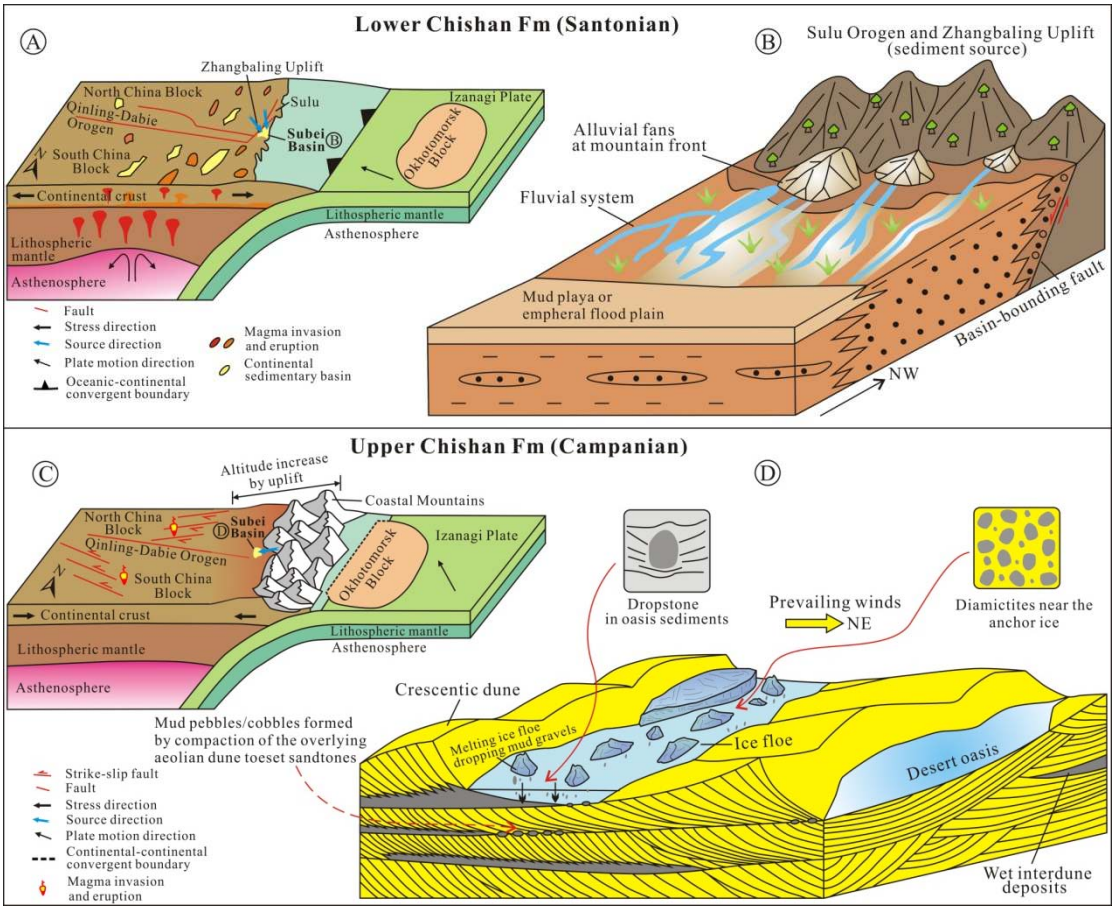

Figure 13. Schematic cartoon model showing the Late Cretaceous tectonic evolution at the East Asian margin. (A) Advancing northwestward subduction of the Izanagi Plate with the development of back-arc rift basins during the period of deposition of the Lower Chishan Formation (Santonian). (B) Depositional model of the Lower Chishan Formation. Alluvial, fluvial and lacustrine deposits were developed in the Subei Basin. (C) Collision of Okhotomorsk Block with Eurasia Plate caused the occurrence of strike-slip fault systems, northwest-southeast shortening, coastal mountains with high elevations, and orogenic exhumation during the period of deposition of the Upper Chishan Formation (Campanian). (D) Depositional model of the Upper Chishan Formation. The Subei Basin turned into a desert basin characterized by aeolian dune and wet interdune

deposits. Cryospheric processes in the East Asian marginal plateau were recorded in the ice-related structures within interdune strata such as dropstones and diamictites.

Table caption

TABLE 1. DESCRIPTION AND INTERPRETATION OF SEDIMENTARY FACIES IN THE CHISHAN FORMATION

Facies association	Facies code	Depositional characteristics	Depositional process
Aeolian dune	Ste	Well-sorted, medium to thick beds, very fine to coarse-grained, trough cross-bedded sandstones (Ste). Internal stratification in the cross-bedded sets comprises grainflow, wind-ripple and grainfall.	Accumulation of crescentic aeolian dune deposits (Hunter, 1977; Kocurek, 1991).
Wet interdune	Sm, Fl	Purple mudstones (Fl) and very fine sandstones (Sm). Decimeter-thick lenticular beds.	A wet interdune element that developed in areas where the interdune depressions suffered fluvial floods (Kocurek, 1981; Mountney and Thompson, 2002).
Damp interdune	Ss	Structureless muddy sandstones. Decimeter-thick lenticular beds.	Deposition in a damp interdune where the groundwater level reached the depositional surface that captured windblown dust and sand grains (Kocurek, 1981).
Dry interdune	Sle	Well-sorted laminated sandstones (She). Decimeter-thick lenticular beds.	Subcritical climbing of wind-ripple strata on the dry depositional surface (Kocurek, 1981).
Aeolian sandsheet	She	Well-sorted, horizontal to sub-horizontal laminated fine sandstones (Sle and She). Medium to thick beds.	Subcritically climbing translatent strata of wind ripples (Hunter, 1977; Kocurek, 1981).
Fluvial channel deposits	St, Sl, Fl	Trough cross-bedded sandstones (St), low-angle cross-bedded	Downstream migration of sand bars in ephemeral fluvial channel settings (Miall, 1977; Todd, 1989; Allen et al.,

		sandstones (Sl) and thinly bedded or lenticular purple mudstones (Fl). Several meters to tens of meters wide. Tabualr bodies with erosive bases. Fining-upward units.	2014).
Overbank flood deposits	Sm, Fl	Interbedded massive tabular sandstones (Sm) and laminated mudstones (Fl) without erosive bases. Fining-upward units. Pale grey-green mottling, silty aggregates and slickensides in the meter-scale thick massive mudstone layers	Unconfined flow deposition that characterizes overbank flood deposits (Smith et al., 1989; Miall, 1996). Floodplain environments during high-magnitude floods (Retallack, 1994; Basilici et al., 2022).
Lake deposits	Gh, Sm, Sl, Fl	Siltstones and mudstones (Fl), with massive muddy sandstones (Sm) and minor horizontal to low-angle cross-bedded laminated sandy conglomerates (Gh) and lenticular low-angle cross-bedded sandstones (Sl). Occurrence of mudcracks fossilized root traces, burrows, ostracodes, and charophytes.	A shallow lake to offshore setting (Benvenuti, 2003; Scherer et al., 2007; Frisch et al., 2019).

[1]Supplemental Material. Description of measure sections. Detailed analytical procedures. Detrital zircon U–Pb signals of potential sources. Figure S1. Tables S1–S5. Supplemental references. Please visit https://doi.org/10.1130/XXXX to access the supplemental material, and contact editing@geosociety.org with any questions.